Diplomarbeit

Pump-controlled light emission from micro and random lasers

ausgeführt am

Institut für Theoretische Physik
der Technischen Universität Wien

unter der Anleitung von

Prof. Stefan Rotter
Dipl.-Ing. Matthias Liertzer
durch

Thomas Hisch
Schweidlgasse 6/19
A-1020 Wien
t.hisch@gmail.com

_____   _____
Datum   Unterschrift

Contents

Chapter 1.

Introduction

More than fifty years ago the laser has been invented and has since then given rise to a large variety of different applications, in diverse fields such as consumer electronics, information technology, medicine, law enforcement, entertainment, and the military. The applications in these numerous fields build on the interesting properties of lasers and the low cost of these special light sources [1].

Numerically, laser structures can be studied efficiently with the recently developed steady state ab-initio laser theory (SALT), first formulated by Türeci et. al. in 2006 [2, 3]. Before the SALT complex laser devices often required explicitly time-dependent simulations, which easily become computationally very demanding for lasers in the semi-classical limit ($kR \gg 1$). With the steady state formulation, however, only a time-independent problem needs to be solved self-consistently. The availability of such an efficient laser simulation tool opens up many possibilities for the investigation of complex lasing devices which were previously out of reach [4].

One interesting problem of this kind is related to recent experiments which demonstrated that deformed micro cavity lasers feature directional modes which emit only into certain preferred directions. In certain applications directional emission of light is important due to its energy efficiency, i.e., light is only emitted into directions where it is desired and not elsewhere. The investigated deformed cavities include limacon-shaped [5–7], quadrupole-shaped [8] and elliptical-shaped [9] micro cavities. In these cavities the direction into which the laser emits light are given by the shape and the index of refraction of the cavity and so far can only be changed by mechanically tuning the two-dimensional cavity or some mirrors.

The emission characteristics of a laser are, however, determined by both the cavity shape and the spatial profile of the applied external pump. The pump profile can thus also be used to influence or shape selected laser modes [10, 11]. The problem is that the higher the quality factor of the cavity the lower the influence of the pump profile on the laser modes. Deformed micro cavity lasers are thus in general not suited for shaping laser modes with the pump profile due to their high index of refraction.

Therefore, instead of studying deformed micro cavity lasers, an exotic and promising type of lasers that feature a low quality factor is investigated in this thesis, i.e.,

so-called random lasers. They are subject to intensive research because they feature lasing behavior although the media of random lasers are disordered [12, 13]. If these lasers are in the weakly scattering regime, defined by a mean free path larger than the size of the system, the pump profile has a strong impact on the modes and can therefore be used to shape the laser modes at will. Spatial light modulators (SLM) have opened up new possibilities to implement such mode-shaping in the laboratory [14–17].

In this thesis we try to tackle the fundamental difficulty of directional emission from random lasers into desired directions by only spatially shaping the pump profile. For simplicity we first study 1D cavities to gain basic insights about the control over laser emission. In a next step we move on to the more interesting 2D random lasers. To obtain directional emission of light, optimization algorithms are employed to find the optimal pump configuration. This is a very challenging problem especially in the two-dimensional case where the parameter space is huge.

Chapter 2.

Theoretical Background

In this chapter we give an overview over the recently developed steady-state ab-initio laser theory (SALT) [2]. This theory provides the multi-periodic solutions of the Maxwell-Bloch (MB) equations, which are the key equations of semiclassical laser theory [18]. The SALT-framework allows us to solve the MB equations without an explicit time-dependence and thereby provides the tools to numerically study the lasing properties of large cavities in a reasonable amount of time. Furthermore, we present two commonly used basis sets, which can be used to solve the main equation of the SALT.

2.1. Steady-state ab-initio laser theory

The SALT builds on the semiclassical laser theory in which the electromagnetic field is treated classically and only the interaction with the gain medium is treated using quantum mechanics. SALT not only successfully describes the lasing modes at and above threshold of arbitrarily complex geometries, but also predicts the output power of each mode and the structure of the electromagnetic field inside and outside the cavity. The term 'ab-initio' in the SALT acronym refers to the fact that the only input parameters are the dielectric function of the system and the gain curve. Compared to previous laser theories SALT is computationally much more efficient due to its time independent formulation.

The gain medium is modeled by an ensemble of uniformly distributed two-level emitters with a level-spacing of $\hbar\omega_a$. This model is only valid for atoms where the level spacing is quite different from the differences between any other energy levels and where the energy level pertubation due to the external field is not too strong [18]. The basis of the SALT is given in terms of the MB equations,

$$\nabla^2 E^+ - \varepsilon_c(\mathbf{x})\ddot{E}^+ = 4\pi\ddot{P}^+ \tag{2.1a}$$

$$\dot{P}^+ = -(i\omega_a + \gamma_\perp)P^+ + \frac{g^2}{i\hbar}E^+ D \tag{2.1b}$$

$$\dot{D} = \gamma_\parallel(D_0(\mathbf{x}) - D) - \frac{2}{i\hbar}E^+\left[(P^+)^* - P^+\right]. \tag{2.1c}$$

This set of coupled nonlinear spatio-temporal differential equations describes the light-matter interactions using the inversion D, the nonlinear polarization of the gain medium P and the electric field E. In this thesis we only consider TM polarized waves such that we can treat the fields as scalar quantities. For example, in the case of two-dimensional cavities the fields point in the direction perpendicular to the cavity ($\boldsymbol{E}(\mathbf{x},t) = E(\mathbf{x},t)\boldsymbol{e_z}$, $\boldsymbol{P}(\mathbf{x},t) = P(\mathbf{x},t)\boldsymbol{e_z}$).

Equation (2.1a) is the telegraph equation, where the polarization acts as a source term and ϵ_c is the dielectric function of the host material. The fields E^+ and P^+ denote the positive frequency components[1] of the corresponding real valued fields E and P. The relaxation rate of the polarization is denoted by $\gamma_\perp$ and conforms to the width of the homogeneously broadened gain curve. The second relaxation rate is the one of the inversion D and is denoted by $\gamma_\parallel$. The other parameters of the MB equations (2.1) are the frequency of the gain center ω_a and the dipole matrix element g.

The cavity is pumped by an external source which leads to a population inversion of the atoms in the gain medium. It should be noted that SALT does not include how this inversion comes about. The inversion D relaxes at a rate $\gamma_\parallel$ to a stationary inversion D_0, which we will refer to as the pump from now on. For a detailed derivation of the MB equations (2.1) with the employed rotating wave approximation (RWA) see [3, 18, 19].

The ansatz for the derivation of steady state equations is that the electric field and the polarization are multi-periodic in time,

$$E^+(\mathbf{x},t) = \sum_{\mu=1}^{N} \Psi_\mu(\mathbf{x})e^{-ik_\mu t}, \tag{2.2a}$$

$$P^+(\mathbf{x},t) = \sum_{\mu=1}^{N} p_\mu(\mathbf{x})e^{-ik_\mu t}, \tag{2.2b}$$

where Ψ_μ are the a priori unknown lasing modes and k_μ the unknown lasing frequencies. In this ansatz N denotes the number of active lasing modes at a certain pump D_0. Note that we set $c = 1$ ($k = \omega$).

The central SALT equation in differential form is derived by inserting the multi-periodic ansatz (2.2) into the MB equations (2.1) (for a complete derivation see [19]) and is given by,

$$\left[\nabla^2 + k_\mu^2 \left(\varepsilon_c(\mathbf{x},k_\mu) + \underbrace{\frac{\gamma_\perp}{(k_\mu - k_a) + i\gamma_\perp} \frac{D_0(\mathbf{x})}{1 + \sum_{\mu'} \Gamma_{\mu'}|\Psi_{\mu'}|^2}}_{\epsilon_g(\mathbf{x},\{k_\nu,\Psi_\nu\})} \right) \right] \Psi_\mu(\mathbf{x}) = 0, \tag{2.3}$$

---

[1] $E = E^+ + E^-$, $P = P^+ + P^-$

where $\Gamma_{\mu'}$ is short for $\Gamma(k_{\mu'}) \equiv \gamma_\perp^2/(\gamma_\perp^2 + (k_{\mu'} - k_a))$, which is the homogeneously broadened gain curve. This gain curve is of Lorentzian shape, determined by the central frequency k_a and the FWHM $2\gamma_\perp$. For a chosen gain curve the frequency dependent dielectric function of the host material $\varepsilon_c(k, \mathbf{x})$ can be assumed to be frequency independent in the k-range of the gain curve, provided that the width of the curve is not too large. In this thesis we neglect its k-dependence completely.

The differential equation (2.3) has the form of a Helmholtz equation with a dielectric function, consisting of a passive (ε_c) and an active (ε_g) part, the latter describing the response from the gain medium. The total index of refraction of this Helmholtz equation is $n = \sqrt{\varepsilon_c + \varepsilon_g}$. The active dielectric function ε_g includes a sum over the spatial profiles of all active laser modes in its denominator. This nonlinear denominator fixes the actual intensities of each mode to a well-defined value and describes the physical effect of spatial hole burning [18]. As each mode depends only on the absolute values of all other modes, mode-locking cannot be described in the present version of the SALT.

In order to calculate the multimode solution of the central SALT equation a self-consistent iterative solution algorithm can be employed [19, 20]. As we are only interested in the first lasing mode Ψ_0, multimode lasing has not been pursued in this thesis.

At threshold, i.e., where the gain equals the losses of the system, the general nonlinear SALT equation (2.3) simplifies to a linear differential equation, because there the intensity of the first lasing mode and the nonlinear term $\propto |\Psi_\mu|^2$ both vanish to zero,

$$\left[\nabla^2 + k_\mu^{(t)2} \left(\epsilon_c(\mathbf{x}, k_\mu^{(t)}) + \frac{\gamma_\perp D_0(\mathbf{x})}{(k_\mu^{(t)} - k_a) + i\gamma_\perp} \right) \right] \Psi_\mu^{(t)}(\mathbf{x}) = 0. \qquad (2.4)$$

The solutions of Eq. (2.4) are called the threshold lasing modes (TLMs). Each TLM $(k_\mu^{(t)}, \Psi_\mu^{(t)})$ is connected to a specific pump strength $D_{0,\mu}^{(t)}$ at which the TLM starts to lase while neglecting any other mode above threshold. The very first TLM requires the smallest pump strength D_0.

If the pump profile does not change during the pump process one can write the stationary inversion $D_0(\mathbf{x})$ as the product of a real-valued positive pump-strength D_0 and a normalized pump profile $F(\mathbf{x})$,

$$D_0(\mathbf{x}) = D_0 F(\mathbf{x}), \text{ where } \int F(\mathbf{x})\, d\mathbf{x} = 1. \qquad (2.5)$$

This allows us to compare the required pump threshold D_0 of the first laser mode for different pump profiles and for different cavities.

2.2. Solutions of the Threshold SALT equation

In semiclassical laser theory [2] quasi-bound (QB) modes have been used to treat modes of open high-Q cavities. These modes are solutions of the Helmholtz equation $[\nabla^2 + n(x)^2 k_m^2]\varphi_m = 0$, where the eigenvalue k_m^2 is complex due to the openness of the cavity. This complex frequency k_m results in a divergent and therefore unphysical behavior of these modes outside the cavity. As long as the cavities have a high quality factor QB modes describe the spatial profiles of the laser modes well within the cavity [19]. However, modes of lasers with low-Q resonators cannot be described with QB states and therefore a different set of states has to be used [19, 21].

The TLM pairs $(k_\mu^{(t)}, \Psi_\mu^{(t)})$ can be determined by scanning the external frequency k in Eq. (2.4) and by checking at which point of k the pump-strength D_0 turns real. D_0, which is then the eigenvalue of Eq. (2.4), can turn real for multiple frequencies k and for multiple eigenstates. The state with the lowest positive value of D_0 is referred to as the first TLM, the one with the second smallest value of D_0 as the second TLM and so forth.

2.2.1. Constant flux states

The most common method for solving the SALT Eqs. (2.3) is to expand the solutions $\Psi_\mu(\boldsymbol{x})$ in terms of a natural basis set, which is the set of the so-called constant flux (CF) states [2, 22],

$$[\nabla^2 + \varepsilon_c(\mathbf{x})k_n^2(k)]\varphi_n(\mathbf{x}, k) = 0, \quad \mathbf{x} \in \mathcal{C} \tag{2.6a}$$

$$\left[\nabla^2 + n_0^2 k^2\right]\varphi_n(\mathbf{x}, k) = 0, \quad \mathbf{x} \notin \mathcal{C}. \tag{2.6b}$$

From Eq. (2.6b) it follows that the energy-flux far outside the cavity $\mathcal{C}$ is conserved, since both the external wave-vector k and the constant index of refraction of the environment n_0 are real. k_n is the complex eigenvalue of the CF state equation Eq. (2.6a) and needs to have a negative imaginary part such that the solutions are amplifying inside the cavity [2]. In addition to the differential equation (2.6) we require that the CF states are purely outgoing waves far outside the cavity as the actual laser modes have the same property, which translates to the boundary condition for the CF states,

$$\partial_r \varphi_n(\mathbf{x}, k) \overset{|\mathbf{x}| \to \infty}{=} in_0 k\varphi_n(\mathbf{x}, k). \tag{2.7}$$

In order to implement this boundary condition we introduce the last scattering surface (LSS). The LSS is a convex hull, which has the property that light propagating out of it cannot reenter. This requires that the index of refraction outside the LSS is constant such that light is not backscattered. The cavity $\mathcal{C}$ can be chosen at will as long as it is enclosed by the LSS (even disjoint), with the simplest choice

being the interior of the LSS. In 1D the LSS coincides with the outer ends of the cavity.
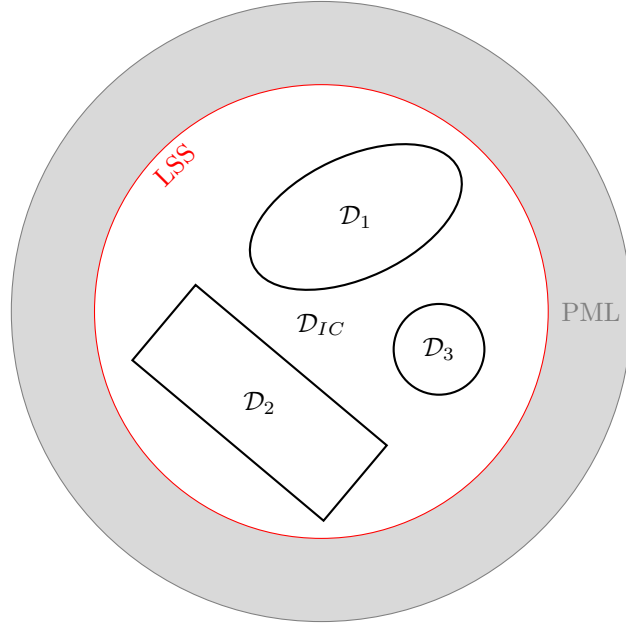
Figure 2.1.: Last scattering surface (LSS) of an example laser system consisting of three cavities which are denoted by the domains $\mathcal{D}_1$, $\mathcal{D}_2$ and $\mathcal{D}_3$. The domain $\mathcal{D}_{IC}$ is the intercavity region. The gray area denotes the PML (see text) used to implement the boundary condition (2.7).

If we impose the boundary condition (2.7) directly on the LSS we would restrict the outgoing waves to be perpendicular to the LSS, which is unphysical. With the help of perfectly matched layers (PML) we introduce a ring-shaped finite-sized absorbing layer connected to the LSS so that we may simply set the wave function to zero at the outer end of this layer. The absorbing layer effectively represents a transition from one material to another, which should generally cause reflection from the boundary, however the PML is specified in such a way that these back reflections are completely suppressed [20].

To employ the CF states in the SALT equations (2.3) and (2.4) the solutions φ_n and their derivatives have to be continuous at the boundary of the cavity $\mathcal{C}$ for TM polarized waves. The eigenvalues of the CF state equation (2.6) are parametrized by the external frequency k. For simple one-dimensional cavities these eigenvalues and the corresponding states can be obtained analytically [19] and for simple profiles of the refractive index (see inset of Fig. 2.2 (a)) the eigenvalues of the CF states show a simple dependence on the frequency k. However, if we consider more complex

spatial profiles of the index of refraction like the one in Fig. 2.2 (b), the scattering coefficients of the passive cavity may feature a resonant behavior that is also reflected in the k-dependence of the eigenvalues.
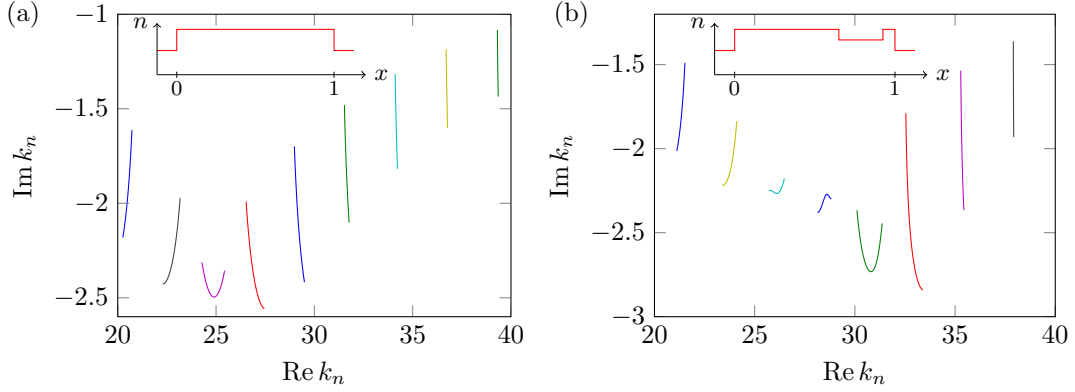
Figure 2.2.: Eigenvalues of the frequency parametrized CF states. The insets show the index of refraction n of the two cavities. In both cases the domain of the cavity is set to $\mathcal{C} := [0, 1]$. Inside the cavities the index of refraction is $n = 1.2$ and the index of the little notch in (b) is $n_n = 1.1$. The length of the notch is tuned to $L_n = m\pi/(n_n k)$, where k was set to 30 and the mode index m to 3. Each line in (a) and (b) shows an eigenvalue k_n parametrized by the outgoing frequency k in the range $[27, 33]$.

The open (non-Hermitian) boundary condition (2.7) implies that the CF states are biorthogonal on the domain $\mathcal{C}$ with respect to the relation

$$\int_{\mathcal{C}} \varepsilon_c(\boldsymbol{x}) \varphi_n(\boldsymbol{x}, k) \varphi_m(\boldsymbol{x}, k) \, \mathrm{d}\boldsymbol{x} = \delta_{nm} \alpha_n, \qquad (2.8)$$

where α_n are the normalization constants.

Typically a large number of CF states are required (~ 200 [3]) to obtain the laser modes as well as the TLMs with a spatially varying pump profile, because the pump profile does not enter the CF equation. To reduce the number of necessary basis states a new basis set has been introduced [3, 19], which is the set of the so-called threshold constant flux (TCF) states.

2.2.2. Threshold constant flux states

An alternative basis set for the expansion of the laser modes is given by the so-called threshold constant flux (TCF) states [3],

$$[\nabla^2 + (\varepsilon_c(\mathbf{x}) + \eta_n(k)F(\mathbf{x}))k^2]u_n(\mathbf{x}, k) = \qquad 0, \quad \mathbf{x} \in \mathcal{C}, \qquad (2.9a)$$

$$\left[\nabla^2 + n_0^2 k^2\right] u_n(\mathbf{x}, k) = \qquad 0, \quad \mathbf{x} \notin \mathcal{C}, \qquad (2.9b)$$

where η_n denotes the TCF eigenvalue and $F(\mathbf{x})$ is the pump profile. The advantage of this definition over the conventional definition of CF states is that each TLM corresponds to a single TCF state, whereas for CF states a linear combination is in general needed to obtain a good approximation of a TLM. By comparing Eq. (2.9) with Eq. (2.4) and employing Eq. (2.5) we can derive the necessary condition for a TCF state to be equivalent to a TLM [3]

$$\eta[k_\mu] = \frac{\gamma_\perp D_{0,\text{th}}^{(\mu)}}{k_\mu - k_a + i\gamma_\perp}, \qquad (2.10)$$

where $D_{0,\text{th}}^{(\mu)}$ is the real threshold pump strength of the μ-th TLM. This complex condition can be rewritten in the form of two real equations [4]

$$(\text{Re}\,\eta)^2 + \left(\text{Im}\,\eta + \frac{D_{0,\text{th}}^{(\mu)}}{2}\right)^2 = \frac{D_{0,\text{th}}^{(\mu)\,2}}{4}, \qquad (2.11a)$$

$$\frac{\text{Im}\,\eta + D_{0,\text{th}}^{(\mu)}}{\text{Re}\,\eta} = \frac{k_\mu - k_a}{\gamma_\perp}. \qquad (2.11b)$$

The remarkable feature of these equations is that only the second one depends on the gain curve ($k_a, \gamma_\perp$). One can interpret Eqs. (2.11) graphically: Eq. (2.11a) describes a circle in a complex plane with radius $D_0/2$ and with a central point at $-iD_0/2$ (see Fig. 2.3). The possible solution of Eq. (2.11) at the origin ($\eta = 0$) has to be rejected because of the diverging frequency k of the solution at this eigenvalue.

For every point B that depends on the frequency k on this circle a line can be drawn that goes through the points A and B of Fig. 2.3. If the slope of this line is equal to $\frac{k_\mu - k_a}{\gamma_\perp}$ then the TCF state at a frequency k_μ and with eigenvalue η at the point B corresponds to a TLM. The TLM with the smallest real pump strength D_0 is the first TLM. The biorthogonality relation of the TCF states is given by [3]

$$\int_\mathcal{C} F(\mathbf{x})u_n(\mathbf{x}, k)u_m(\mathbf{x}, k)\,\mathrm{d}\mathbf{x} = \delta_{nm}\alpha_n, \qquad (2.12)$$

where α_n are the normalization constants which are used to normalize the TCF states.
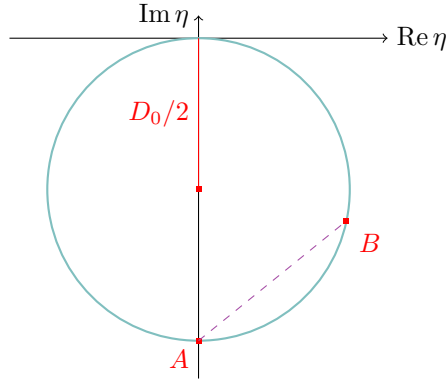
Figure 2.3.: Graphical representation of Eq. (2.11) (see text). Every TCF state that is equivalent to a TLM needs to fulfill the two equations in (2.11). The circle is centered at $-iD_0/2$ with a radius $D_0/2$. The point A is fixed at $-iD_0$ and the point B is located at the intersection of the circle with a the line of slope $(k_\mu - k_a)/\gamma_\perp$ emanating from point A (see Eq. (2.11b)).

2.2.3. Directional characteristics of a laser mode

The main topic of this thesis is the directional emission profile of a laser mode. It can be calculated with the help of the energy flow which is given by the real part of the complex pointing vector $S(\mathbf{x})$ (see Eq. (2.13)) in the farfield [23],

$$\text{Flux}(\varphi) := \lim_{r \to \infty} r \operatorname{Re} [\mathbf{S}(r, \varphi, k_\mu)] = \lim_{r \to \infty} \frac{r}{2k_\mu} \operatorname{Im} \left[\Psi_\mu^*(r, \varphi) \partial_r \Psi_\mu(r, \varphi) \right], \qquad (2.13)$$

and is denoted by the label 'Flux' in the figures of this thesis.

Chapter 3.

One-dimensional edge-emitting laser-cavities

In this chapter we explore the possibility of controlling the emitted radiation of a one-dimensional ridge laser by changing the applied pump profile. We will see that pump profiles, which lead to emission to the left or to the right, can be found for arbitrary one-dimensional cavities as long as the refractive index contrast is small. Additionally we show that for high-Q cavities with a large index contrast directional emission is possible when the passive modes themselves display a directional behavior.

3.1. Low-Q cavities

One-dimensional conventional high-Q lasers like laser pointers are constructed such that they emit laser-light in only one direction. The electromagnetic-field oscillates between two mirrors of an optical cavity and escapes with a probability defined by the reflectivities of the mirrors of the resonator. The directionality of the light is due to the difference of the reflectivities of the two mirrors. One mirror is usually perfectly reflective ($R = 1$) while the other one has a reflectivity that is a little smaller than 1. The properties of the laser-light of such a simple system can be studied with the famous rate-equations [24]. If one is interested in the actual electric field of the laser modes of the system the SALT equations (2.3) need to be solved which include the index of refraction, the pump profile and the properties of the gain curve. The difference of the mirrors translates to an asymmetric refractive index $n(x)$ of the system that is important for the directionality in high-Q resonators.

In this section we want to show that we can make a low-Q laser to emit in one direction only even if the index of refraction of the passive cavity is totally symmetric. In section 2.1 we have shown that the total index of refraction of the laser consists of two parts namely the passive dielectric function $\varepsilon_c(x)$ and the active dielectric function $\varepsilon_g(x)$, that contains the pump profile $F(x)$. If we are able to find a special pump profile that induces an asymmetric total index of refraction of the laser, the first laser-mode will be directional. Such pump profiles need to feature

steps at a scale smaller than the wavelength inside the cavity in order to build up mirrors that reflect the photons.

A good measure for the directionality of a laser-mode in a one-dimensional system is the asymmetry A that is defined as

$$A = \frac{I_L - I_R}{I_L + I_R}, \tag{3.1}$$

where I_L and I_R denote the intensity of the mode on the left and on the right of the cavity. A can only take on values that are in the interval $[-1, 1]$. Due to this definition symmetric modes like the one obtained in Fig. 3.2 have zero asymmetry.

We consider the following geometry with an active medium with index n_g and length L_c embedded into the medium of the environment with index n_e. For simplicity we take $n_g = n_e = 1$ which describes a cavity with zero index-contrast.
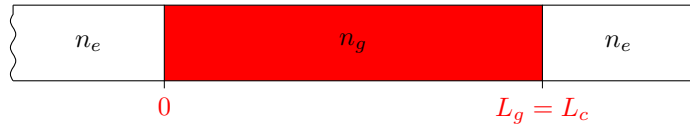
Figure 3.1.: Geometry of a simple one-dimensional edge-emitting laser cavity of length L_c that is open at both leads. The index of refraction of the gain medium is n_g and that of the environment is n_e. In this simple case the length of the gain medium L_g is equal to the total length of the cavity L_c.

If we pump the system uniformly ($F(x) = 1$) the emitted radiation is equally emitted into both directions due to symmetry reasons as can be seen from Fig. 3.2.

To obtain the desired asymmetric modes with $A \approx \pm 1$, we use a minimum search algorithm to find the optimal pump-configuration such that the first TLM emits solely to the right ($A \approx -1$). We expand the pump profile $F(x)$ in terms of orthonormal basis functions on the interval $[0, L_c]$

$$F(x) = \sum_{i=0}^{N} \alpha_i \tilde{P}_i(f(x)), \quad \forall x \in [0, L_c] \tag{3.2}$$

where $\tilde{P}_i$ are the normalized Legendre-polynomials, $f(x)$ is an affine transformation from $[0, L_c]$ to $[-1, 1]$ and α_i is a set of complex coefficients. The transformation $f(x)$ is required because the polynomials P_i are orthogonal on $[-1, 1]$ with respect to the L^2 norm. Note that the expansion in Eq. (3.2) allows negative values for the pump. Since, this would correspond to absorption of light inside the cavity where $F(x) < 0$, we only allow coefficients α_i for which

(a)

(b)
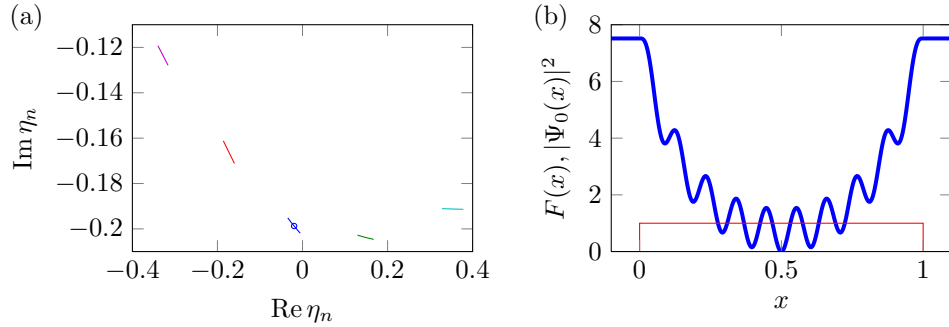
Figure 3.2.: TCF-eigenvalues $\eta_i(k)$ (left) of a cavity with $n_g = n_e = 1$ and length $L_c = 1.0$ (Fig. 3.1). Each line shows the eigenvalues parametrized by the outgoing frequency k in the range $[k_a - 3\gamma_\perp, k_a + 3\gamma_\perp]$. The eigenvalue of the TCF state which corresponds to the first TLM is marked with a blue circle and turns on to lase at a threshold $D_0 = 0.2$ at an external frequency $k = 29.99$. The pump profile $F(x)$ (red) and the intensity of the first TLM (blue) is shown on the right. The Lorentzian gain curve has a median frequency $k_a = 30.0$ and a FWHM of 0.2.

$$\int_{\mathcal{C}} F(x)\,\mathrm{d}x = 1 \quad \text{and} \quad F(x) \geq 0 \quad \forall x \in \mathcal{C}. \tag{3.3}$$

The normalization of the pump profile $F(x)$ in Eq. (3.3) is required in order to compare the TCF eigenvalues η (see Eq. (2.9)) and hence the thresholds of the first laser modes D_0 (see Eq. (2.4)) for different pump configurations.

We use a simple local optimization algorithm of *MATLAB*, which tunes the coefficients α_i such that the pump configuration leads to a first TLM with an asymmetry A as close to -1 as possible.

Starting with a randomly chosen initial pump configuration the optimization algorithm obtains a final asymmetry of -0.9999 (see Fig. 3.3). The resulting final pump profile has a discontinuity at the left side ($x = 0$) that leads to a reflectivity of $R = 0.029$ on this side. However, on the right side there is no visible discontinuity of the pump profile and therefore the reflectivity is zero. This small but important reflectivity difference is the cause of the good asymmetry A. For the calculation of the reflectivities R_L (left side) and R_R (right side) we have used [24],

$$R_L = \left| \frac{n_g(x=0) - n_e}{n_g(x=0) + n_e} \right|^2 \quad \text{and} \quad R_R = \left| \frac{n_g(x=L_c) - n_e}{n_g(x=L_c) + n_e} \right|^2, \tag{3.4}$$

where $n_g(x)$ is the refractive index of the active system that is equal to $\sqrt{\varepsilon_c + \eta F(x)}$ (see Eq. (2.9)) and n_e is the index of the environment. The obtained directional first
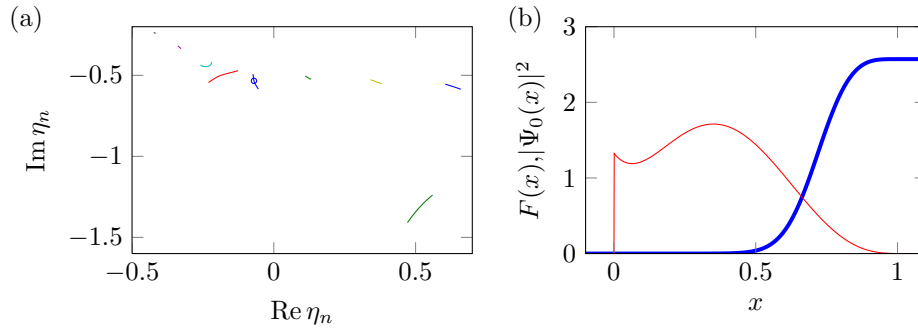
Figure 3.3.: Effect of the minimization of the asymmetry A on the first TLM (b,blue) and on the TCF-eigenvalues (a) using a basis consisting of 6 Legendre-polynomials for the pump profile (b,red) (compare Eq. (3.2)). The geometry is shown in Fig. 3.2. The eigenvalues (a) are obtained with the final pump configuration and are parametrized by the outgoing frequency k in the range $[k_a - 3\gamma_\perp, k_a + 3\gamma_\perp]$. The blue circle in (a) marks the TCF eigenvalue of the first TLM. The minimization algorithm stopped after 761 iterations with a final asymmetry of -0.99999 of the first TLM at the frequency $k = 29.987$ with a threshold $D_0 = 0.54$.

TLM has a threshold D_0 of 0.54 at the external frequency $k = 29.987$. The reason for the small oscillation of the pump profile around $x = 0.1$ in Fig. 3.3 is not well understood yet.

There exist modes with an even higher asymmetry A than the one obtained for the first TLM in Fig. 3.3(b). These so-called surface modes feature a mode profile, which is dominated by anisotropic exponential growth inside the cavity [25]. The intensity of such modes on either the left or the right side outside the cavity is orders of magnitude higher than on the other side, thus their asymmetry is either $+1$ or -1. Unfortunately, we can't bring the surface modes to lase first because their threshold is too high compared to the threshold of the other modes. The k-parametrized TCF-eigenvalue $\eta(k)$ on the bottom of Fig. 3.3(a) corresponds to a such a surface mode. The first TLM (b), however, features a much lower threshold as can be seen from the smaller distance of the TCF-eigenvalue to the origin in (a) (see Section 2.2.2), even if its mode profile has an almost exponential growth inside the cavity. The reason for this is that its intensity at the left side is small but non-zero and thus does not correspond to a surface mode.

We conclude that for low-Q cavities the required reflectivity difference between the left and right end of the cavity is given by the jump in the index of refraction, which is imposed by the pump profile. An analytical pump profile which also fulfills this requirement is, e.g., an exponential function $F(x) = C(e^{\beta(x-1)} - 1)$ vanishing

at $x = 1$ and with a sharp cut-off at the cavity boundary ($x = 0$). The exponentially shaped pump profile with the best asymmetry is determined by scanning the parameter β (see Fig. 3.4). The asymmetry of the first TLM which we obtain in this way is almost as good as the asymmetry obtained before with the optimization algorithm (Fig. 3.3).

In our calculations we observe that at the thresholds D_0 of the first laser-modes (see Figures 3.2-3.4) the asymmetry is better the higher the threshold, which means that we need to pump the system more intensively to get asymmetric modes than to get symmetric modes. The fact that the asymmetric modes feature a higher threshold compared to the symmetric modes is due to the leakiness of the asymmetric pump-induced cavity on the right side (see Figs. 3.3(b) and 3.4(b)). Therefore the asymmetric modes require a higher gain to equal the losses of the system. It is not yet understood why the threshold of the first TLM in Fig. 3.3 is almost 1.5 times as high as the threshold in Fig. 3.4.
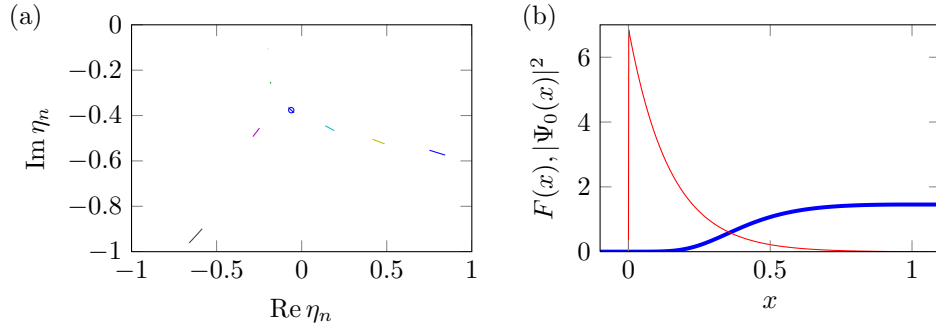
Figure 3.4.: TCF-eigenvalues (a) and first TLM (b,blue) with an exponential pump profile $F(x) = C[\exp(6.85(x-1)) - 1]$ (b,red). The obtained asymmetry ($A = -0.9996$) is almost as good as the one obtained with the minimization algorithm (Fig. 3.3). The geometry used was the same as in Fig. 3.2. The first TLM has a threshold $D_0 = 0.39$ at an external frequency k of 29.984. The scanned k-interval for the eigenvalue plot is $[k_a - 3\gamma_\perp, k_a + 3\gamma_\perp] = [27.7, 30.3]$. The eigenvalue of the TCF state at $k = 29.984$ which corresponds to the first TLM is marked with a blue circle.

If we slightly increase (up to $n_g = 1.1$) the constant index of refraction of the gain medium of the geometry depicted in Fig. 3.1 we are still able to induce directional TLMs but the final asymmetry gets worse for higher refractive indices. At high index contrasts we are no longer able to control the asymmetry with the pump due to a strong preference of symmetric cavity modes. This can be understood by considering the minor contribution of the pump $D_0(\mathbf{x})$ to the total dielectric

function $\varepsilon_c + \varepsilon_g$ in (see Eq. (2.3)). It follows that in the high-Q regime the modes are mostly determined by the geometry of the passive cavity.

3.2. High-Q cavities

As it is not possible to induce by the applied pump directional laser modes in one-dimensional symmetric resonators with high Q-values, new concepts are required to achieve this goal. The idea which we propose is to consider cavities which feature two nearby passive modes with different directionalities. The purpose of the pump profile is then to select one of these directional cavity modes for lasing. Note that this concept is different from the low-Q case, where only the shape of the pump profile determines the properties and directionality of the laser-modes. The important topic to address is thus the design of a cavity such that it features modes with different directionality.

The resonator of the previously mentioned laser pointer consists of two mirrors with different reflectivities, that lead to emission of laser-light into a single direction. What we want for our resonator are mirrors that change their reflectivities in dependence of the frequency k. At one frequency k_R the resonator should emit light only in the right direction, at another nearby frequency k_L the emission should be directed to the left side.

Mirrors with such properties can be constructed by successively connecting dielectric layers with alternating refractive indices, which exhibit a high reflectivity at a certain frequency due to destructive interference of light inside the layers. Sequences of dielectric layers that operate on the basis of destructive or constructive interference are called Bragg layers or Bragg reflectors [26]. Usually, these Bragg layers are tuned to either optimal reflectivity (high reflectance coatings) or optimal transmittance (anti-reflection coatings). If we require that these layers perfectly reflect light ($R \approx 1$) as well as perfectly transmit light ($R \approx 0$) at frequencies that are close to each other then we need to carefully choose the lengths and/or the refractive indices of the dielectric layers.

To construct a cavity that fulfills this requirement we take the single cavity from Fig. 3.1 and attach Bragg reflectors to both ends of it. We have to choose different Bragg reflectors on either side because their reflectivities need to be very different at the frequency k_L as well as at k_R. This guarantees that the cavity modes at these frequencies feature a highly asymmetric emission profile. The resulting cavity is shown in Fig. 3.5 and consists of three materials each with a different index of refraction.

For the construction of this resonator we set the lower index of refraction to $n_L = 1$ and the higher one to $n_H = 5$. The original cavity has a length of $L_g = 1$ and an index of refraction of $n_g = 3.6$ (see the plot at the bottom of Fig. 3.7). Therefore its
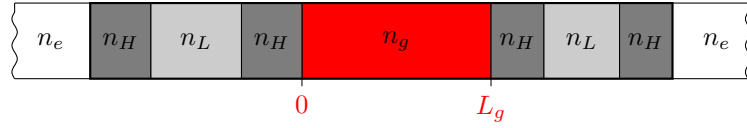
Figure 3.5.: Geometry of a one-dimensional laser consisting of a gain-medium (red) with index n_g, length L_g and Bragg layers with indices n_L, n_H on the left and right side. The lengths of the Bragg layers on both sides are slightly different to achieve the desired spectral properties of the layers (see text). The index of the environment is n_e.

passive cavity frequencies are given by $k_m = m\pi/(n_g L_g)$. The length of the individual layers of the Bragg reflectors are chosen such that the maximum/minimum of the respective reflectivities is reached at two adjacent resonance frequencies k_m, k_{m+1} (see Fig. 3.6).

In order to induce directional modes at these frequencies that have an almost equal lasing threshold we center the Lorentzian gain curve between the passive cavity modes. The directional modes need to have an almost equal laser threshold such that each of them can be selected as the first laser mode by spatially adapting the pump profile to the energy density of the corresponding mode. This almost equal threshold of our directional modes is required in order to operate mode-switching by spatially adapting the pump profile to the mode with either asymmetry $A \approx +1$ or $A \approx -1$. In this way the laser prefers to lase at the desired frequency due to the reduction of the threshold of one mode compared to the threshold of the other mode. Note that with this procedure we are only able to select between directional modes that are pre-defined by the geometry of our laser resonator.

The difficulty of this approach is that the laser needs to favor the directional modes over the non-directional modes, which accordingly need to have a higher threshold, otherwise the emitted light would in general not be directional.

If the peak gain frequency is directly in the middle between the cavity resonances and the system is uniformly pumped then two directional modes start to lase first (see Fig. 3.7). These two TLMs almost have the same threshold as expected. However, the actual lasing frequencies of these TLMs are not the frequencies k_m and k_{m+1} but can be found somewhere between the cavity resonances and the peak gain frequency k_a (Fig. 3.6) due to laser line-pulling.

From the theory of optical resonators [1, 27] it is known that if the reflectivities of both sides of a one-dimensional resonator are close to 1 at a certain frequency then standing waves emerge, provided that these waves fit into the resonator. Despite the high reflectivities of both Bragg reflectors at the frequency of k_a there is no laser-mode with a frequency close to k_a, because the length L_g is not a multiple of
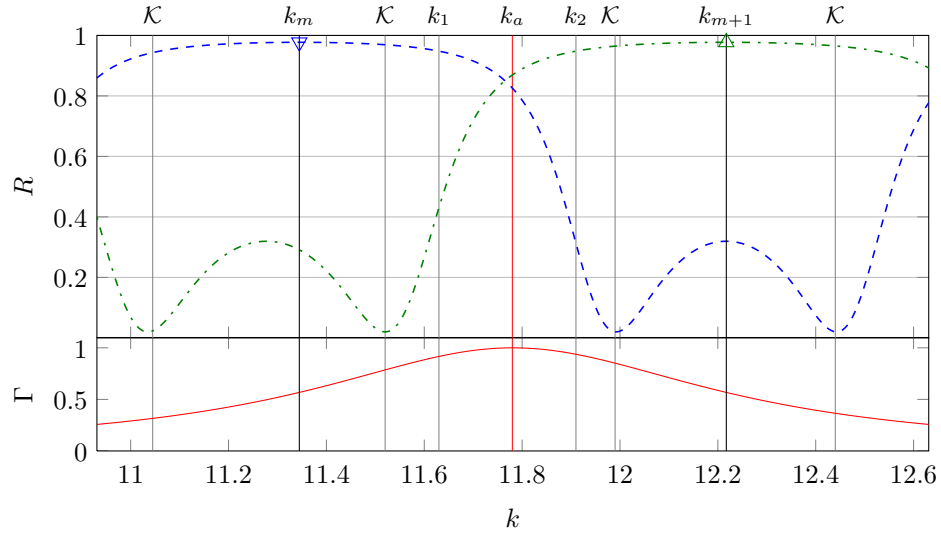
Figure 3.6.: Reflectivities R_L (blue, dashed) and R_R (green, dash-dotted) as a function of the frequency k. The gain curve Γ has a FWHM of $2\gamma_\perp = 0.5$ and is plotted in red. The peak gain frequency was set to be in the middle between two passive cavity modes (see text; $k_a = 11.7808$). The maximum of the reflectivity of the Bragg reflector on the left side is at the frequency $k_L = k_m = 11.3446$ and the maximum on the right side is at $k_R = k_{m+1} = 12.217$) where we chose $m = 13$. The first two threshold laser modes turn on at $k_1 = 11.63$ with asymmetry $A = -0.878$ and at $k_2 = 11.91$ with asymmetry $A = 0.901$. The frequencies where the difference $|R_L - R_R|$ features maxima are denoted by $\mathcal{K}$.

half of the corresponding wavelength.

In contrast to the TCF eigenvalues of simple low-Q cavities studied in section 3.1, the eigenvalues of our laser with a high-Q resonator (Fig. 3.7 (a)) strongly depend on the properties of the Bragg reflectors as can be seen in Figs. 3.8 and 3.9. A property of the eigenvalues of the parametrized first two TCF states which turn into the first two TLMs at the frequencies k_1 and k_2 is that the imaginary part features minima as a function of the real part (see Fig. 3.8). These minima correspond to the "leaky" surface modes at the frequencies $\mathcal{K}$ (Fig. 3.6) requiring a large amount of gain to bring them to lase. By comparing Fig. 3.8 with Fig. 3.9 one can see that due to the fact that the difference between the reflectivities R_L and R_R at the frequencies $\mathcal{K}$ is maximal the absolute value of the asymmetry parameter A is maximal as well.

In addition to the minima of the imaginary parts of the TCF eigenvalues in Fig. 3.8 there are also local maxima (denoted by ① - ③) in the vicinity of the frequencies
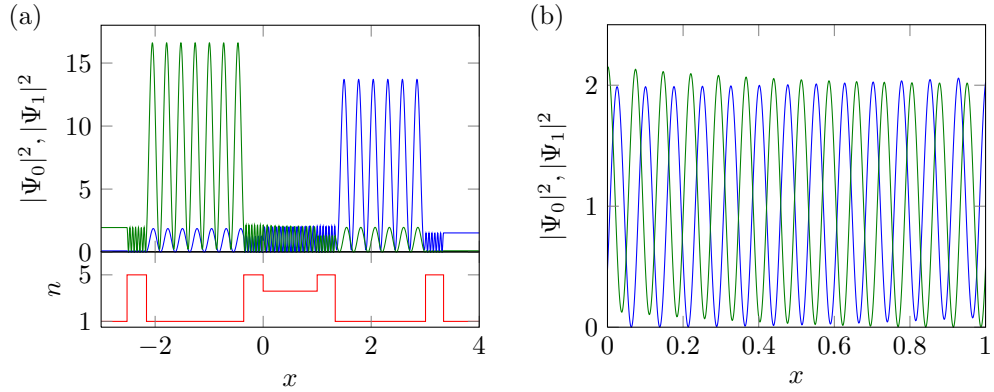
Figure 3.7.: The first two TLMs of a laser (see Fig. 3.5) when the gain-medium is pumped uniformly. At the bottom of (a) the index of refraction of the cavity is shown. The properties of the gain curve are described in the caption of Fig. 3.6. The laser frequency of the first TLM is $k_1 = 11.63$ (blue) and the frequency of the second is $k_2 = 11.9$ (green). The thresholds of these modes are $D_1 = 0.18$ and $D_2 = 0.20$. A zoom of the profiles of the modes is shown in (b).

k_a ②, k_{m+1} ③ and k_m ①. These maxima represent modes which are more strongly bound (due to the reflectivity difference $|R_L - R_R|$ (see Fig. 3.6) at these frequencies) than the surface modes inside the cavity. However, they have a slightly smaller absolute value of A (see inset of Fig. 3.9). The TCF states corresponding to these maxima would turn on as one of the first (threshold) laser modes if their TCF eigenvalue had a very small real part compared to the imaginary part (This is discussed in detail in chapter 4). Since, however this is not the case only the eigenvalues marked with a circle (see Figs. 3.8 and 3.9) turn on as the first two TLMs.

3.2.1. Mode-switching

Considering the energy density $|\Psi(x)|^2$ of the first two TLMs inside the cavity (see Fig. 3.7) we observe that the wavelength of both modes is almost the same within the gain region $x \in [0, 1]$ (see Fig. 3.7 (b)) and that the nodes of the profiles of one mode coincide with the anti-nodes of the profile of the other mode. We can thus select each of the two modes by using the corresponding energy density as the pump pattern $F(x)$.

If we set the pump configuration to the energy density of the first TLM (k_1) $F(x) = C \cdot |\Psi_0(x)|^2$ of Fig. 3.7 and normalize it (see Eq. (3.3)), then this TLM stays
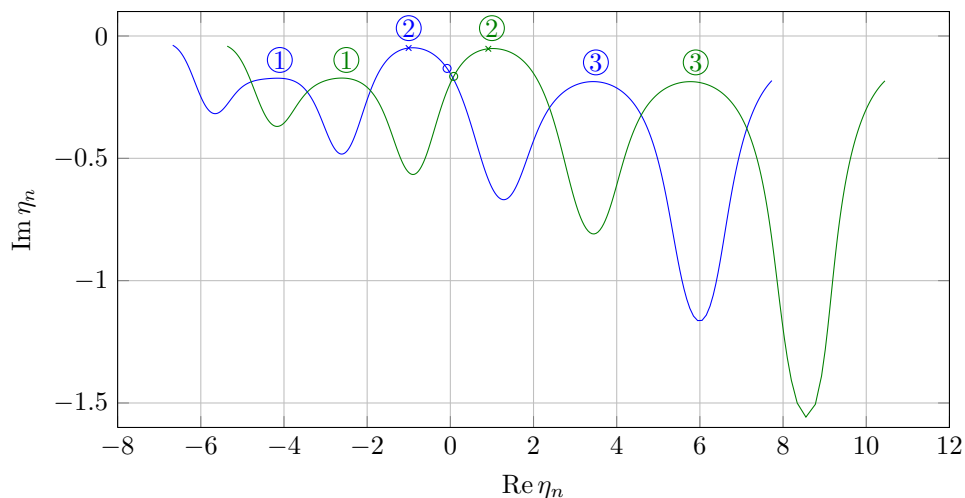
Figure 3.8.: TCF state eigenvalues that turn into the very first TLMs as a function of the external frequency k. The blue (green) circle denotes the eigenvalue of the TCF state that corresponds to the first (second) TLM. The crosses mark the eigenvalues at $k = k_a$. The external frequency k is in the range $[k_a - 3.4\gamma_\perp, k_a + 3.4\gamma_\perp]$. The numbers in the circles mark the frequency regions where the imaginary parts of the parametrized eigenvalues (as a function of the real parts) feature local 'maxima'.

the same (see Fig. 3.10 (a)) but also has a smaller threshold ($D_1 = 0.12$) compared to the threshold obtained with uniform pump ($D_1 = 0.18$, see caption of Fig. 3.7) due to the spatial concentration of the pump profile on this mode. The second non-interacting laser mode (k_2) is the same as for uniform pump (same frequency and same asymmetry), but its threshold goes up from $D_2 = 0.2$ to $D_2 = 3.3$. The threshold of the second real (interacting) laser mode would go even further up due to spatial hole-burning.

If the second TLM (k_2) (Fig. 3.10 (b)) is set as the pump profile the order of the first two TLMs in the uniform pump case switches, i.e., the mode at k_2 becomes the first lasing mode and the one at k_1 the second TLM. Here, the threshold of the obtained first TLM (k_2) decreases from $D = 0.2$ (uniform pump) to $D_1 = 0.13$, whereas the threshold of the second TLM at the frequency k_1 again increases from $D = 0.18$ to $D_2 = 0.28$.

Note that the shown pump profiles and the TLMs in Fig. 3.10 are normalized with respect to two different norms: The pump profile satisfies Eq. (3.3), whereas the TLM, as it is equivalent to a TCF state, is normalized with respect to the TCF biorthogonality relation (2.12). This explains the different amplitudes of the profiles
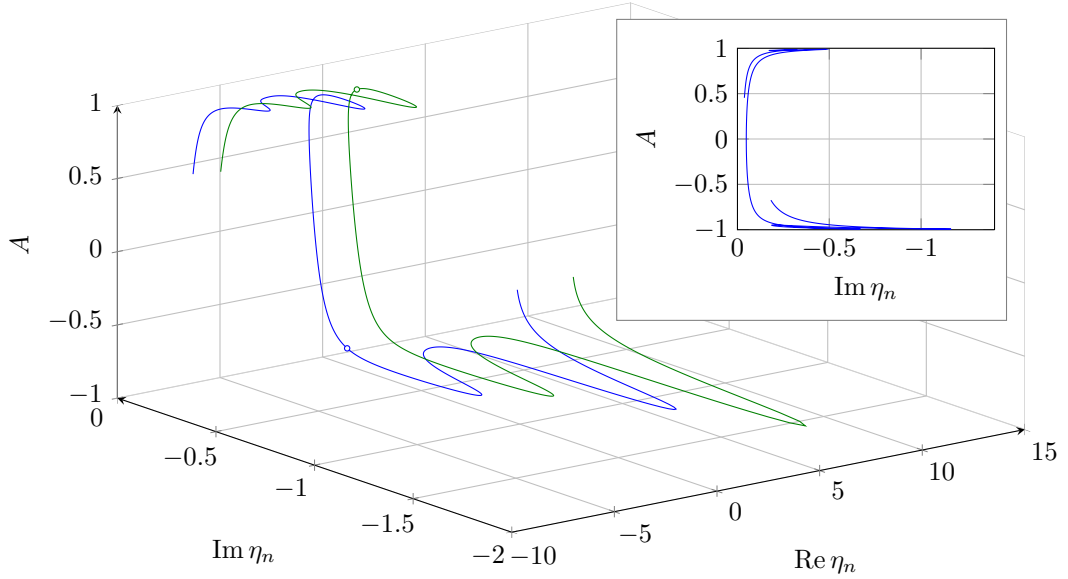
Figure 3.9.: 3D version of Fig. 3.8 that shows the dependence of the asymmetry A on frequency dependent eigenvalues η of the TCF states. As in Fig. 3.8 the blue (green) circle denotes the eigenvalue of the TCF state that corresponds to the first (second) TLM. The minima of the imaginary parts of the eigenvalues (see text) have the best absolute value of the asymmetry A. The inset shows the asymmetry of the modes corresponding to the parametrized TCF state (first TLM) as a function of the imaginary part of η.

in Fig. 3.10. Apart from that, the external frequency k of the obtained first TLMs is equal to the frequency of the desired modes used in the pump profiles. This proves that mode selection in specific high-Q cavities is possible and that it works surprisingly well.

3.2.2. Summary

In high-Q cavities directional emission of light can not be observed by only changing the pump profile if the cavity is symmetric and has a high index-contrast. In lasers with asymmetric high-Q cavities featuring directional modes, however, it is possible to select one of these modes by setting the pump pattern to the energy density of the desired directional mode. This works as long as the threshold of the directional modes is almost the same and lower compared to the threshold of the symmetric modes of the system.

(a)

(b)
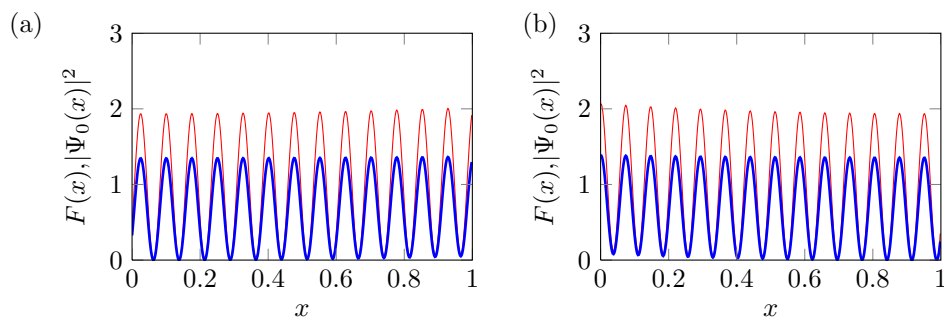
Figure 3.10.: Spatial profile of the first threshold laser modes (blue) when the first (a) and second (b) TLM of Fig. 3.7(b) was set as the pump profile (red). The first TLM (a) has a threshold $D_1 = 0.12$ and it lases at the frequency $k = 11.63$. The first TLM (b) has a slightly larger threshold of $D_1 = 0.135$ and a lasing frequency of $k = 11.902$. The used geometry of the laser is shown in the bottom of Fig. 3.7(a) and the parameters of the gain curve are given in the caption of Fig. 3.6.

Chapter 4.

Two-dimensional micro-lasers

Our aim is to apply the insights we have gained from the study of one-dimensional cavities to the much more interesting case of two-dimensional cavities. In this chapter we investigate a relatively new kind of lasers, so-called random lasers, in which gain is introduced in a random aggregate of scatterers. Even such disordered structures emit laser light by means of coherent multiple scattering as was shown in multiple experiments [12, 28]. However, the emitted radiation of random lasers is in general not directional. Here we tackle the fundamental difficulty of directional emission from random lasers by spatially shaping the pump profile.

We first discuss the geometry of a random laser and state that depending on the elastic mean free path of the system and its size the laser can be in three different scattering regimes. In addition to that we differentiate between lasers where the parts that provide the gain are different. Later on we investigate modes of random lasers that are either in the weakly or strongly scattering regime. In the latter regime we discuss the mode profiles for different pumping schemes, whereas in the case of weakly scattering random lasers we try to create new modes for different spatial pump profiles. Furthermore we check if we can analytically determine a pump configuration leading to a directional laser mode. In the final section of this chapter we employ an optimization algorithm to find a pump profile for a weakly scattering random laser that results in a first laser mode with directional emission.

4.1. Geometry

In order to model a random laser a large number of scatterers is needed and the wavelength of the light should be small compared to the system geometry, corresponding to a large value of kR. The geometry of our modeled random laser consists of a circular-shaped liquid into which non-overlapping square-shaped scatterers are embedded at random positions (see Fig. 4.1). The parts of the laser which provide the required gain can be chosen to be the scatterers, the liquid or both (see Section 4.4). The coverage rate, i.e., the ratio of the total area of the scatterers to the area of the circular-shaped medium of this system is 20%. In a first step the size of these scatterers is chosen small enough to avoid trapping of light within the scat-

terers. In a second step we also investigate what happens if we lift this restriction and choose the scatterer size to be comparable to the wavelength of the light. In this case we find resonances in the scattering coefficients, which are reminiscent of Mie resonances in the case of spherical scatterers.

For technical reasons we study a system where kR is fixed to a value of 30. R is the radius of the disk-shaped medium surrounding the scatterers, which we fix to $R = 1$. The wavelength of the light inside the scatterers is then given by $\lambda_s = \frac{2\pi}{n_s k} \approx \frac{0.21}{n_s}$, where n_s is the refractive index of the scatterers. To avoid that the square scatterers act as resonators we set their diameter[2] d_s to 0.04. This diameter corresponds to a length smaller than a quarter of the wavelength λ_s for an index n_s slightly larger than one. If the index of refraction n_s is increased to values larger than 2, the peaks of the mode profiles are localized inside the scatterers as we show in section 4.4.
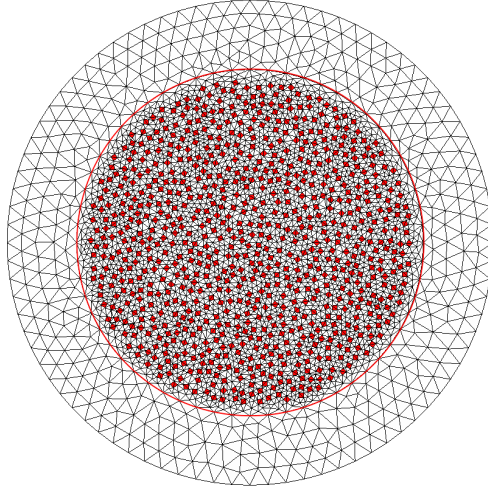
Figure 4.1.: Mesh of a two-dimensional random laser that is used in our simulations. The coverage-rate f_{cov}, i.e, the ratio between the total area of all the scatterers and the area of the circular medium into which the scatterers are embedded is 0.2. The radius R of this circular medium (denoted by the red circle) is 1.0 and the diameter of the square-shaped scatterers d_s is 0.04. The domain outside the red circle is the PML layer (see Fig. 2.1).

---

[2] The side length of the scatterers l_s is given by $l_s = d_s/\sqrt{2}$.

4.2. Weakly and strongly scattering random lasers

In amplifying random media light waves are both multiply scattered and amplified. The characteristic length in the scattering process is the elastic mean free path (MFP) ℓ, which is defined as the average length between two successive scattering events of photons. If the MFP is larger than the size of the system length L, i.e., $\ell > L$, light has a small chance of being scattered and therefore the system is in the quasi-ballistic (or weakly-scattering) regime, because in this regime the light traverses the system on almost ballistic trajectories. If the MFP ℓ is smaller than the system size ($\ell < L$) we enter the chaotic regime, where light is scattered multiple times before leaking out of the system. We note that, for large enough systems, which are presently out of reach for numerics, this chaotic scattering leads to a diffusive regime. Both in the chaotic and in the diffusive regime, the multiple scattering events increase the lifetime of light within the system and thus lower the threshold of the laser modes compared to the case of weak scattering.

When further decreasing the MFP to lengths comparable to the wavelength of light ($\ell \sim \lambda$) localization of light occurs. In this so-called Anderson localization regime or strongly scattering regime modes are confined in a volume/area, the scale of which is given by the localization length ξ. As a result, the modes in this regime feature a high Q factor.

In the random laser under investigation we can study the cross-over between the above regimes by increasing the index of refraction of the scatterers embedded in the random (see Fig. 4.1). Typical mode profiles in each of the three scattering regimes are shown in Fig. 4.2.

In the course of this chapter we are mainly concerned with systems in which the scatterers of the random laser (Fig. 4.1) have an index of refraction of $n_s = 1.2$. According to [29] the MFP of such a system should be about $70R$, which shows that it is in the weakly scattering regime. Even though the scatterers of our cavity have a slightly larger diameter ($d_s = 0.04$) than the scatterers considered in [19] ($d_s = 0.025$) we can assume that the MFP is not much different from $70R$ and that this system is therefore also in the same scattering regime.
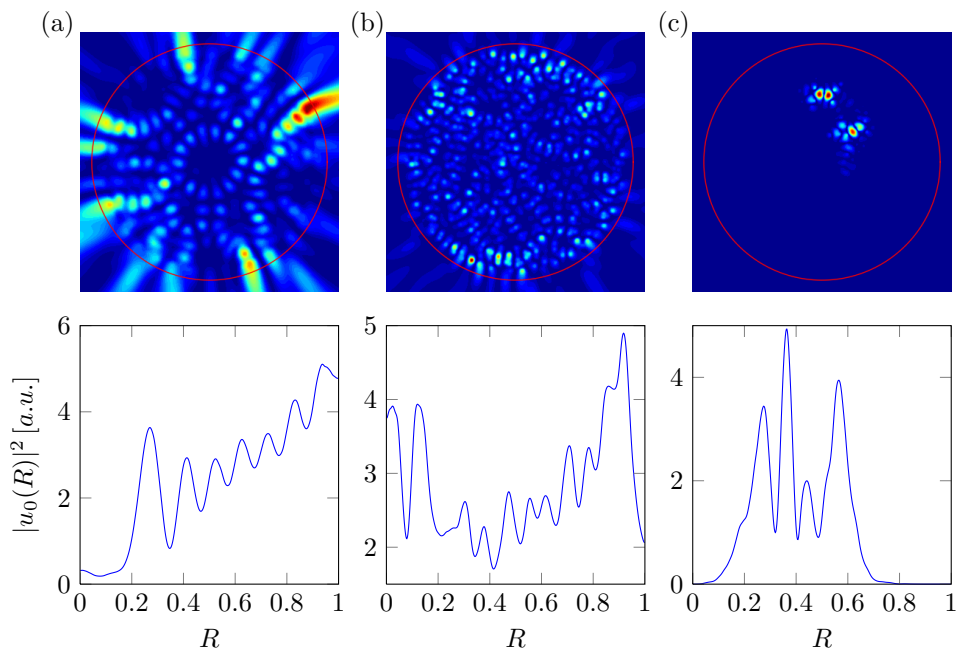
Figure 4.2.: Spatial variation of the first TCF states of a random laser (see Fig. 4.1) with $n_s = 1.2$ (a), $n_s = 2.0$ (b) and $n_s = 3.3$ (c) using a uniform pump profile. The radial profiles of the depicted TCF states are shown below them, which are averaged over all angles φ. No averaging (as in [21]) over a high number of disorder potentials was done to obtain the radial intensity profiles.

4.3. Approximation of TLMs using TCFs for random lasers

Calculating the TLMs of a system depicted in Fig. 4.1 is computationally very expensive especially if they are calculated repeatedly for different pump profiles like in an optimization algorithm. For this reason we assume that the first TLM is given by the TCF state with the smallest absolute value of the eigenvalue η at the gain-center frequency k_a. This means that the eigenvalue of this "first" TCF state has to lie on the imaginary axis, because the imaginary part of the eigenvalue is fixed due to the vanishing right hand side of Eq. (2.11b). Furthermore, to fulfill the circular equation (2.11a) the real part of η has to be zero, which guarantees that the TCF state at the gain-center frequency corresponds to a TLM.

In order to correspond to the first TLM the gain curve needs to be very narrow to avoid that TCF states at other frequencies might turn on as the first TLM. If this is

the case, the TCF state at the frequency k_a with the smallest imaginary part of the eigenvalue η (assuming that the real part is negligible small) is a good candidate for the first TLM.

4.4. Classes of random lasers

In addition to the classification of random lasers according to their mean free path ℓ (see Section 4.2) we also differentiate between three ways in which the random laser provides the gain. In the first class of random lasers both the scatterers and the surrounding medium amplify light. The next class corresponds to lasers where only the scatterers are amplifying and therefore only they need to be pumped as pumping a non-amplifying medium has no effect on the laser modes. In the last class the liquid is amplifying but the scatterers are not. For the study of these laser classes we consider random laser in the weakly scattering regime in the first part of this section. In the last part we discuss how the modes for the different classes change if the laser is in the strongly scattering regime.

Class 1 (gain everywhere): If we pump the scatterers as well as the disk-shaped liquid surrounding these micro particles ($n_s = 1.2$), the mode profile is localized at the boundary of the liquid and has the form of a whispering gallery mode (WGM) (see Fig. 4.3) [9, 30]. This is because there is a little gap between the outermost scatterers and the boundary of the disk-shaped liquid (denoted by a red circular line in Fig. 4.1). The strong fluctuations in the amplitude of the energy-flux profile (Fig. 4.3), defined in Eq. (2.13), are due to the presence of the randomly placed scatterers.

The gap was introduced in the geometry for technical reasons, because the employed mesh generator creates a too fine mesh around the boundary at $R = 1$ when the scatterers are placed close to this circular cavity-PML boundary. Computationally, it is therefore more efficient to introduce this spacing as the number of finite elements of the employed mesh is then considerably smaller.

Due to this gap a pump-induced cavity [25] can be formed that confines light as we have already seen in the study of one-dimensional low-Q cavities (Sec. 3.1). The step of the uniform pump profile at $R = 1$ and the size of the gap determines the structure of the whispering gallery modes. We emphasize, however, that such a behavior is artificial and is very unlikely to appear in reality. At higher thresholds, i.e., larger absolute values of the eigenvalue η of the TCF states, the system features TCF states which are not whispering gallery type modes. However, these states are very unlikely to lase as the low-threshold WGMs are always preferred.

We can avoid the appearance of these high-Q WGMs as the first TCF state by pumping the system only up to a certain critical radius $R_{cut} = 0.95$. The used cut radius R_{cut} is chosen such that it coincides with the radius of the outermost scatter-
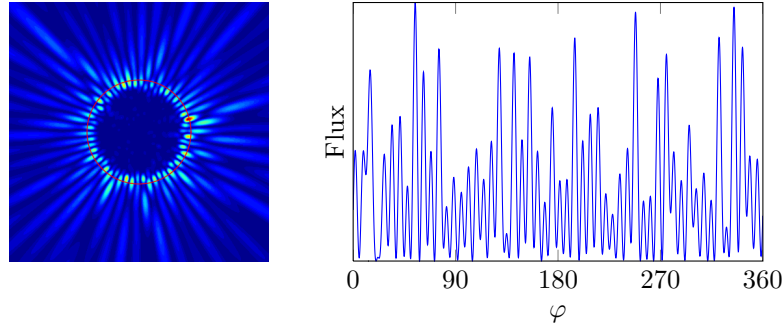
Figure 4.3.: Mode (left) and energy-flux profile (see Eq. (2.13)) of the first TCF state obtained with a uniform pump profile $F(x) = \pi^{-1}$ inside the red circle with radius $R = 1$ using the geometry from Fig. 4.1. The refractive index of the scatterers is $n_s = 1.2$ and the external frequency k is set to 30.

ers. In this way the emergence of the previously mentioned gap is no longer possible (see Fig. 4.4 (a)). We find that the energy-flux profile in (a), defined in Eq. (2.13), is much smoother compared to Fig. 4.3. The brightest regions of the mode profile appear at the edge of the random laser leading to an increasing radial intensity (see Fig. 4.2 (a)) which is characteristic for the weakly scattering regime [21].

Class 2 (only amplifying scatterers): If only the scatterers are pumped then the mentioned gap does not play a role and WGMs do not appear as one of the TCF states of this class. Even if the pump profiles in (a) and (b) of Fig. 4.4 only agree to about 20%, the spatial profiles of the modes correspond to each other surprisingly well.

Class 3 (amplifying liquid but non-amplifying scatterers): In the third and last class only the liquid amplifies light but not the scatterers. The properties of the modes of this class of random lasers are the same as the one of the first class if the pump radius is set to $R_{cut} = 1.0$, i.e., whispering gallery modes emerge. Therefore only the first TCF state is shown in Fig. 4.4(c) for the case that the pump is cut at $R_{cut} = 0.95$. Due to the strong overlap (about 80%) between the pump profiles used in (a) and (c) both the spatial profile as well as the energy-flux profile are almost identical. However, if we further decrease the pump radius to $R_{cut} = 0.93$ and $R_{cut} = 0.91$ the mode profile of the first TCF state changes significantly in all classes (not shown). Therefore we conclude that the similarity between the modes of all three classes is largely related to the disappearance of the scatterers outside of the pumped disk-shaped region ($R = 0.95$) and to the pump cut-off at $R_{cut} = 0.95$. This was verified by only pumping the outer parts of the laser between $R = 0.2$ and $R = 0.95$, i.e., the pump profile F was set to zero in the middle of the cavity. We
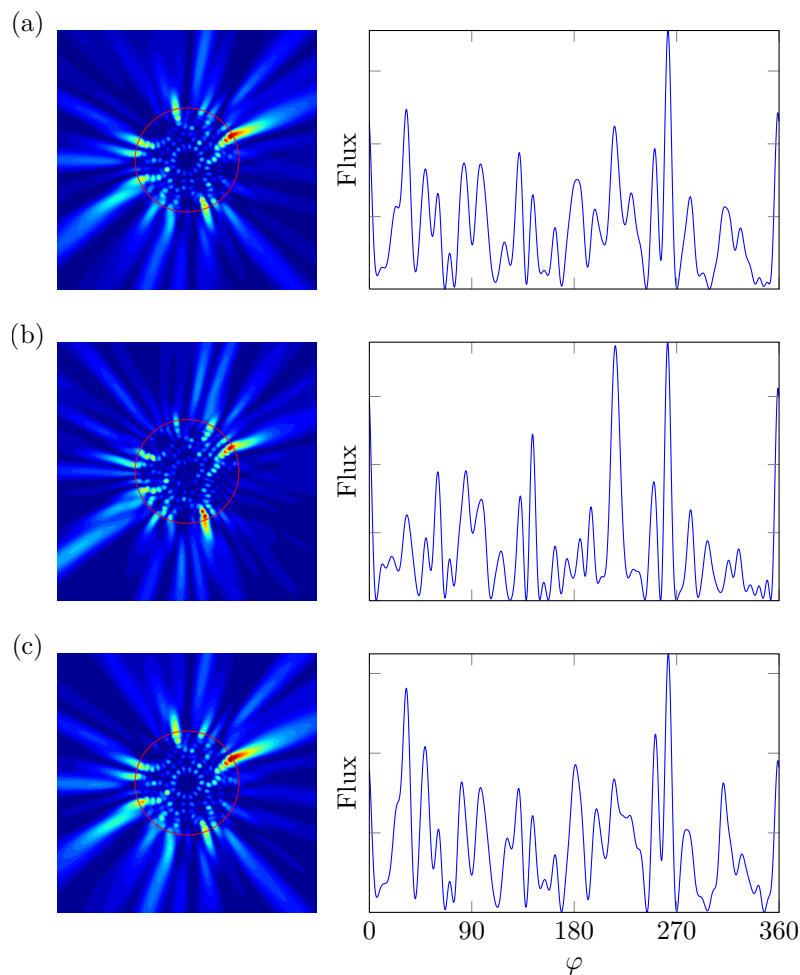
Figure 4.4.: First TCF states and energy fluxes of a random laser with an index of refraction of $n_s = 1.2$ at $k = 30.0$ that is in the weakly scattering regime. The used pumping classes are: both the scatterers and the space between them is pumped up to the critical radius $R_{cut} = 0.95$ (a), only the scatterers (b) and only the space between scatterers is pumped up to $R_{cut} = 0.95$ (c).

found for all classes that if we pump the system with this spatially restricted pump profile the mode profile is almost the same as in Fig. 4.4.

4.4.1. Random lasers in the strongly scattering regime

At the beginning of this chapter we mentioned the fact that the scatterers could trap light if the size of the scatterers is at the scale of the wavelength. As we can draw some interesting physical conclusions we discuss the random laser (Fig. 4.1) in the strongly scattering regime here. To enter the strongly scattering regime we set the index of the scatterers to $n_s = 3.3$. Thus, the ratio of the wavelength of the scatterers to their diameter λ_s/d_s for the considered refractive index and the size of the scatterers is 1.6, meaning that the diameter is larger than half the wavelength. Due to the small ratio λ_s/d_s the shape of the scatterers plays an essential role for the creation of the modes. If we had used circular scatterers with the same diameter, the mode profiles would be different.

The TCF states in the strongly scattering regime for the mentioned three different classes are depicted in Fig. 4.5. To understand why the real parts of the eigenvalues of these TCF states are very large compared to their imaginary part and hence do not correspond to the first TLM (see Section 4.3) we need to introduce the gain-region constant-flux (GRCF) states [25]. These states are defined in the same way as the CF states except that the domain $\mathcal{C}$ in Eq. (2.6) is replaced by the domain of the gain-providing parts of the laser, denoted by $\mathcal{G}$. Therefore they are similar to the TCF states with the advantage that the actual frequency inside the domain $\mathcal{G}$ of the GRCF states is given by the real part of the eigenvalue k_m, whereas it is not clear what the actual frequencies of the TCF states are by only looking at their eigenvalues η_i.

The reason for the large real parts of the TCF-eigenvalues in Fig. 4.5 is due to the large size of the scatterers that lead to the occurrence of certain resonance frequencies. These resonances can be clearly seen from the eigenvalues of the GRCF states in Fig. 4.6(a) and are related to both the average distance between the scatterers and the size of the scatterers.

If only the scatterers act as the gain-region $\mathcal{G}$, there are no GRCF modes around our chosen gain-center frequency of $k_a = 30$ (see Fig. 4.6 (a)). For this reason one can explain why the absolute value of the real part of the eigenvalue of the first TCF state in Fig. 4.5(b) is so large. This is because the real part of η is related to the frequency shift of the TCF state inside the gain/pumped-region. If $\mathrm{Re}\,\eta$ is negative then the interior frequency of the modes is smaller than the external frequency k. If it is positive, also the frequency shift is positive. In addition to that the first TCF state in Fig. 4.5(b) corresponds to a GRCF state with an eigenvalue k_m inside the eigenvalue cluster around $\mathrm{Re}\,k_m = 25$ (see Fig. 4.6 (a)). Therefore the frequency shift from the gain-center frequency is negative and so is the real

part of the TCF state eigenvalue. All the GRCF states in the mentioned cluster around $\text{Re}\,k_m = 25$ have the property that the peaks of their mode profiles are located inside the scatterers, whereas for GRCF states corresponding to the cluster around $\text{Re}\,k_m = 38$ the opposite is the case, i.e., their peaks are located between the scatterers. Finally, the mode profile of the (single) GRCF state with the largest absolute value of the imaginary part $\text{Im}\,k_m = -1$ is localized at the boundary of the random laser and the peaks are inside the scatterers.

In the case of the two other classes (see Fig. 4.5 (a),(c)) the real part of the eigenvalues η is positive corresponding to a shift to a higher frequency than k_a. The eigenvalues of the GRCF states of a system, where only the material/liquid in the space between the scatterers provides gain, are shown in Fig. 4.6(b). As the gap between the scatterers and the circle with radius $R = 1$ (see Fig. 4.1) is part of the gain-region $\mathcal{G}$, WGMs turn up as GRCF states. Most of the depicted eigenvalues (b) correspond to modes with a whispering-gallery type structure. The non-whispering-gallery type modes with peaks between the scatterers are close to the real axis around $k = 43$ and in fact one of these modes is equal to the TCF state shown in Fig. 4.5(c).

The clustering of the GRCF eigenvalues vanishes when we decrease the size of the quadratic scatterers to $l_s = 0.014$ ($d_s = 0.02$) (see Fig. 4.7) [31]. This is because we leave the regime, where the modes are localized inside the scatterers, and enter a regime, where the modes are similar to the one depicted in Fig. 4.2(b).

Returning to Fig. 4.5 we can clearly see that when the entire scattering region is pumped (a) and when only the space between the scatterers is pumped (c) the mode profiles of the first TCF states and their energy fluxes are almost identical. Thus, it suffices to restrict the pump profile to just the liquid to obtain (almost) the same mode as in (a) as the first TCF state. In addition to that the peaks of the mode profiles in (a) and (c) are localized between the scatterers of the random laser. Furthermore the threshold of the mode (c) is lower due to the stronger overlap between the pump profile and the localized mode. Energetically, it is therefore more efficient to only pump the space between the scatterers if one wants to select a mode where the peaks are localized in the space between the scatterers.

If, in turn, we only pump the scatterers (b), the overlap between the pump profile and the mode (a) is not strong enough and therefore a new mode, living inside the scatterers (see inset of Fig. 4.5(b)), turns on as the first TCF state.

(a)

$\eta = 2.58 - 0.00044i$

$|\eta| = 2.575030$

(b)

$\eta = -1.23 - 0.0004i$

$|\eta| = 1.23$

(c)

$\eta = 2.8 - 0.00003i$

$|\eta| = 2.17$

Flux

Flux

Flux

0   90   180   270   360

φ
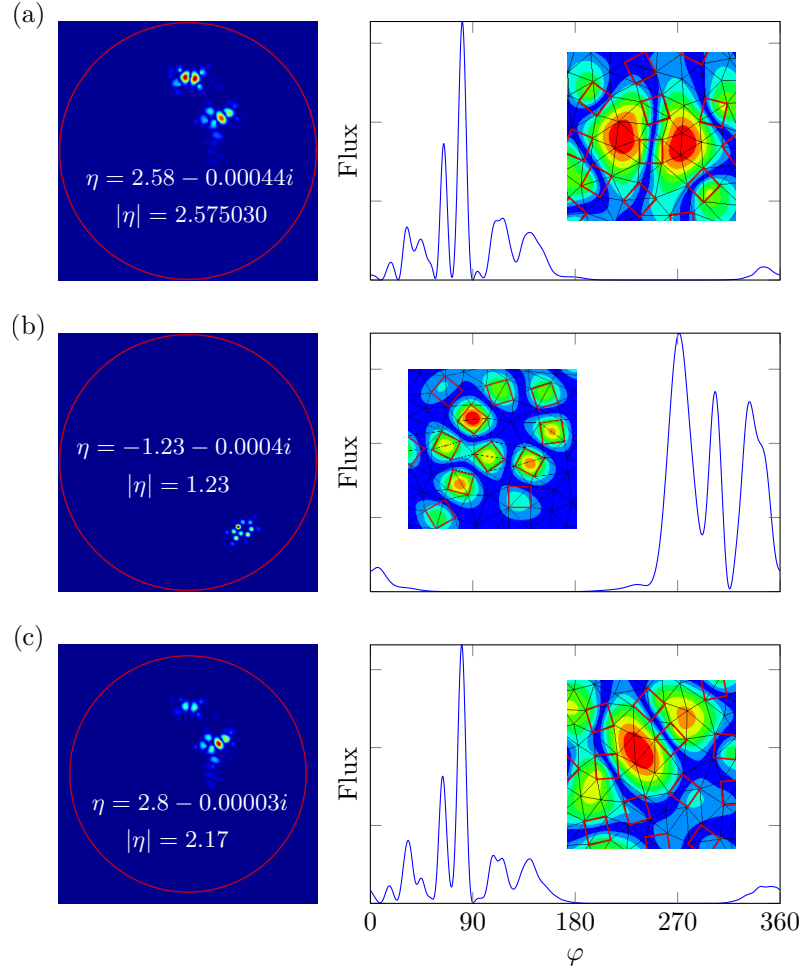
Figure 4.5.: First TCF states and energy flux of random lasers with an index of refraction of $n_s = 3.3$ at $k = 30.0$ (strongly scattering regime). The used pumping schemes are: the entire scattering region up to $R_{cut} = 0.95$ (a), only the scatterers (b) and only the region between the scatterers up to $R_{cut} = 0.94$ (c). The insets in (a)-(c) show zooms of the mode profiles, where the square-shaped scatterers are displayed red.
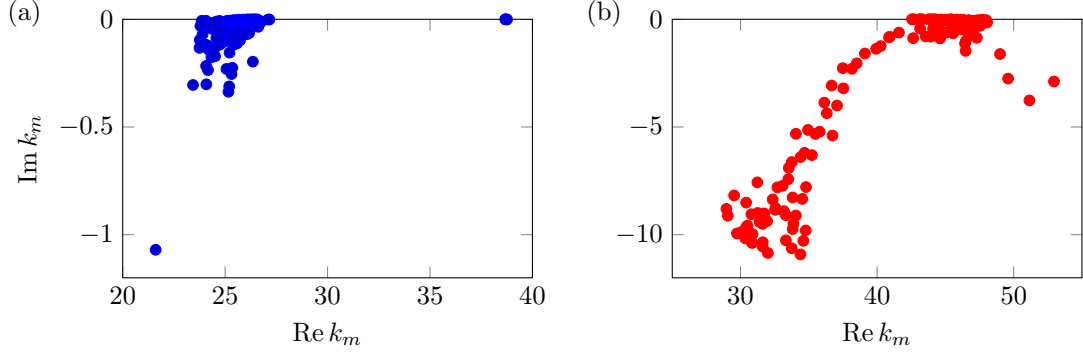
Figure 4.6.: First 150 eigenvalues of the GRCF states around $k_m = 30$ when the gain consists of only the scatterers (a) and only the space between the scatterers (b). The index of refraction of the scatterers is $n_s = 3.3$ and the geometry is depicted in Fig. 4.1. The size of the scatterers is $d_s = 0.04$.
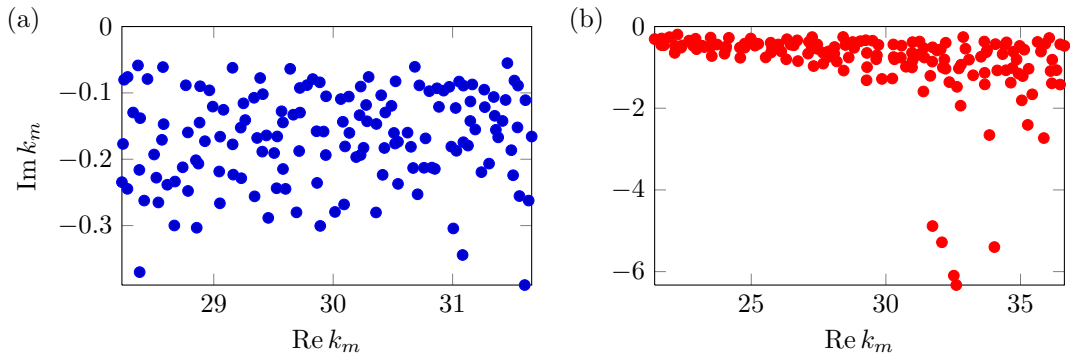
Figure 4.7.: First 150 eigenvalues of the GRCF states around $k_m = 30$ when the gain consists of only the scatterers (a) and only the space between the scatterers (b). The size of the scatterers with $n_s = 3.3$ is set to $d_s = 0.02$.

4.5. Mode selection/creation in weakly scattering random lasers

In the strongly scattering regime one can select modes but not create new modes by spatially shaping the pump profile, because the profile $F(\mathbf{x})$ has a much lower impact on the total dielectric function (see Eq. (2.4)) than the passive dielectric function. Therefore the modes are mostly defined by the spatial variation of the passive dielectric function (for moderate pump strengths). However, in the weakly scattering regime both the scatterers and the pump define the laser modes on a comparable level. In this regime it should thus be possible to create pump-induced modes. For these modes the question is posed whether the pump can also be used to achieve directional emission. Our first idea is to use a linear combination of TCF states of the uniformly pumped system which are superposed such that its emission is directional. If the profile of this constructed state is set as the pump profile one might expect that the mode turns up as one of the TCF states, preferably as the first TCF state.

The artificial state with a directional emission is created by multiplying each of the first 150 TCF states with its inverse phase $-\arg u_i(\mathbf{x}')$ at the chosen point $\mathbf{x}'$ in the far-field,

$$u_{\mathrm{LC}} = \sum_{i=1}^{150} e^{-i\arg u_i(\mathbf{x}')} u_i(r, \varphi; k_a), \qquad (4.1)$$

where the subscript LC stands for linear combination. The point $\mathbf{x}'$ denotes the location where the energy density of the new state u_{LC} should be maximized. Fig. 4.8 shows such a superposed state, where $\mathbf{x}'$ was set to be left of the cavity at $(-5, 0)$. As can be seen the energy density is highest at the left boundary of the cavity (see yellow rectangle in Fig. 4.8). If we want to pump the system with this state we have to restrict it to the parts of the system that provide the gain. Given that we consider a laser, where the scatterers as well as the ambient liquid provide gain, the profile has to be cut at $R_{cut} = 0.95$ (see Section 4.4). The constructed linear combination u_{LC} is, of course, no eigenstate of the TCF eigenvalue problem (2.9) and therefore is not a TCF state, when the pump profile is the same as was used to calculate the u_i equation (4.1).

The pump profile that we use to pump the system is the energy density of the constructed state (see Fig. 4.8) cut at $R_{cut} = 0.95$. The brightest region of the state inside the random laser is located at the left side of the cavity (see the yellow rectangle).

For illustration purposes we study what happens if we pump the system uniformly only inside the yellow rectangle (in addition the pump is cut at $R_{cut} = 0.95$). We observe that modes in which the light traverses the pumped region vertically have a lower threshold than horizontally propagating light (see Fig. 4.9 (b)). This is
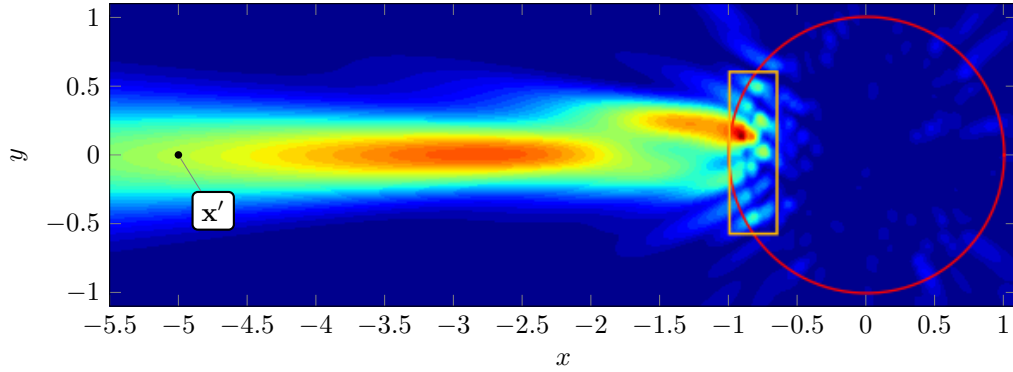
Figure 4.8.: Energy density of the phase coherent superposition of the first 150 TCF states at $k = 30$. For the TCF states the same geometry and the same pump profile was used as in Fig. 4.4(a). The yellow rectangle marks the location where the system has the highest energy density. The $\mathbf{x}'$-node denotes the point where the phases of the TCF states coherently add up.

because light could gather more gain by staying longer inside the pumped region and therefore has a lower threshold. This behavior can even be observed if the pumped rectangular region is placed in the middle of the cavity of the random laser [19].

Also when using the state from Fig. 4.8 as the pump profile, the first TCF state features a mode primarily emitting to the top and to the bottom but not to the desired left side (see energy-flux in Fig. 4.9(c)). We conclude that the presented ansatz doesn't lead to the expected emission profile of the first TCF state.
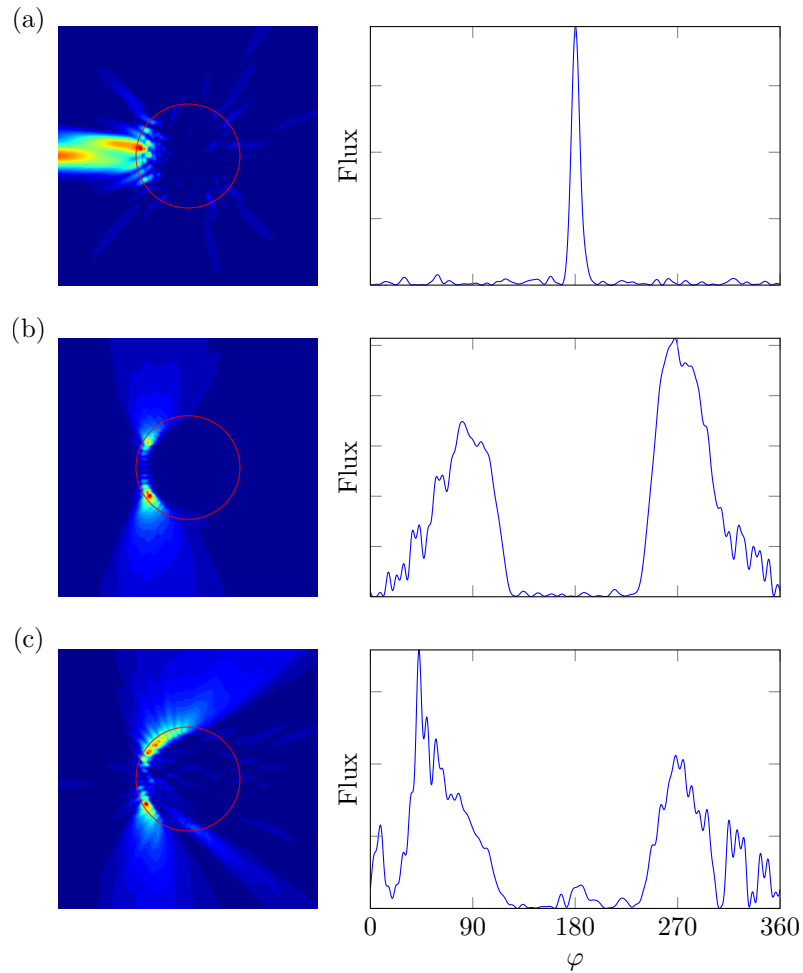
Figure 4.9.: Energy density of the constructed state (a), of the first TCF state when the pump profile is uniform inside the yellow rectangle (see Fig. 4.8) (b) and when the state (a) was set as the pump configuration and cut at $R_{cut} = 0.95$ (b). The corresponding energy-flux of these three states are depicted right to the mode profiles.

4.6. Analytic approach to determine best pump profile

In the previous section we have shown that it is not possible to get a desired mode to lase by using its intensity profile as the pump profile. In this section we try to find an analytic approach to find a pump profile such that this mode becomes an actual laser mode.

   We ask the question whether it is possible to analytically determine the pump configuration leading to a first laser mode with the desired directionality. More precisely, if we construct a directional state by superposing several TCF states as was done in the previous section, we want to find a pump profile such that the superposed state becomes the first TCF state with the lowest threshold.

   The TCF problem Eq. (2.9) has the form of a generalized eigenvalue problem

$$\underbrace{\left(\nabla^2 + k^2 \varepsilon_c\right)}_{A} u_i = \underbrace{-\eta_i k^2 F}_{\lambda_i B} u_i, \tag{4.2}$$

where the operator A includes the index of refraction and B includes the pump profile. Numerically, the matrix corresponding to operator A is complex symmetric but not Hermitian due to the non-Hermitian boundary condition and the matrix corresponding to the operator B is real symmetric and each entry of it is positive[3].

   The state with the desired directionality is given by the linear combination

$$u' = \sum_i \alpha_i u_i, \tag{4.3}$$

with the complex coefficients α_i. As was already mentioned. The goal is to find B' such that u' is the eigenvector with the smallest absolute value of the eigenvalue λ' of the eigenvalue problem

$$Au' = \lambda' B' u'. \tag{4.4}$$

If we insert the definition of u' into Eq. (4.4) we obtain

$$Au' = \sum \alpha_i A u_i = \sum \alpha_i \lambda_i B u_i \overset{!}{=} \lambda' B' u' = \sum \alpha_i \lambda' B' u_i, \tag{4.5}$$

where we have used that u_i is an eigenvector of the original generalized eigenvalue problem (4.2). From Eq. (4.5) it follows that

$$\sum \alpha_i (\lambda_i B - \lambda' B') u_i \equiv 0. \tag{4.6}$$

   At this point we encounter the problem that it is in general not possible to find a pair (λ', B') that fulfills this equation. This is because the eigenstates u_i are linearly

---

[3] We have set $B = F$ and $\lambda = -\eta k^2$.

independent and α_i can be chosen arbitrarily. Therefore $\lambda_i B$ and $\lambda' B'$ have to be equal but this is only possible if the number of states to be superposed is one.

It is thus not possible to find a symmetric operator B' of a non-Hermitian generalized eigenvalue problem such that a linear combination of the eigenstates (using the operator B) becomes an eigenstate of (4.4). Even if this is not possible, there could exist a state which can not be written as a linear combination of TCF states but is directional and emerges as the first threshold laser mode for a certain pump profile.

4.7. Optimization

As we did not obtain satisfactory results with the above two approaches, we now try to employ optimization algorithms similiar to those studied in chapter 3. For 1D cavities we expanded the pump profile in terms of Legendre polynomials and then optimized the coefficients such that the resulting first TLM features minimal value of the asymmetry A. For 2D cavities we have to define a new measure for the directionality, choose a good two-dimensional basis for the pump profile and devise a clever optimization algorithm.

4.7.1. Measure of the directionality

In order to determine the directionality of a 2D laser we, in principle, calculate the ratio of the amount of laser light emitted into a predefined small angular window over the amount of laser light emitted into all directions. For this, we define the directionality $\mathcal{D}$ by the functional

$$\mathcal{D}[u_0] := \frac{\int_0^{2\pi} G(\varphi) \mathrm{Flux}(u_0, \varphi) \, d\varphi}{\sqrt{\int_0^{2\pi} G^2 \, d\varphi \int_0^{2\pi} \mathrm{Flux}^2 \, d\varphi}}. \tag{4.7}$$

This definition incorporates the function G representing the far-field pattern that we wish to achieve and the function Flux, which is the energy-flow profile, defined by equation (2.13), of the first TCF state u_0 at the frequency k

$$\mathrm{Flux}(u_0, \varphi) := \lim_{r \to \infty} r \operatorname{Re}\left[\mathbf{S}(r, \varphi, k)\right] = \lim_{r \to \infty} \frac{r}{2k} \operatorname{Im}\left[u_0^*(r, \varphi) \partial_r u_0(r, \varphi)\right].$$

The normalization term in the denominator of equation (4.7) guarantees that the maximal and thus best obtainable value of the measure $\mathcal{D}$ is 1 and the lowest is 0. The main reason why we introduced the normalization term is that different pump profiles could induce TCF states which have the same energy-flux profile (see Section 4.4.1) and therefore the (unnormalized) overlap integrals $\mathcal{D}$ of these states are

the same. This could impede the convergence of optimization algorithm justifying the normalization in Eq. (4.7).

In our calculations we use for the optimal far-field emission a Gaussian function $G(\varphi; \varphi_c, \delta) = \exp \frac{-(\varphi - \varphi_c)^2}{4 \ln 2 \delta^2}$ centered at $\varphi_c = 180°$ and with a FWHM of $\delta = 11.7°$. As an example we show the energy flux of two arbitrary TCF states and the chosen Gaussian reference far-field pattern in Fig. 4.10. The depicted energy flux features a different directionality $\mathcal{D}$ in these two cases. Even if the directionality of the second profile looks promising its value of the measure $\mathcal{D}$ is low, which is due to the visible side lobes and due to the little shift of the peak in the middle relative to the reference peak, resulting in a reduced overlap $\mathcal{D}$ of only 0.47.
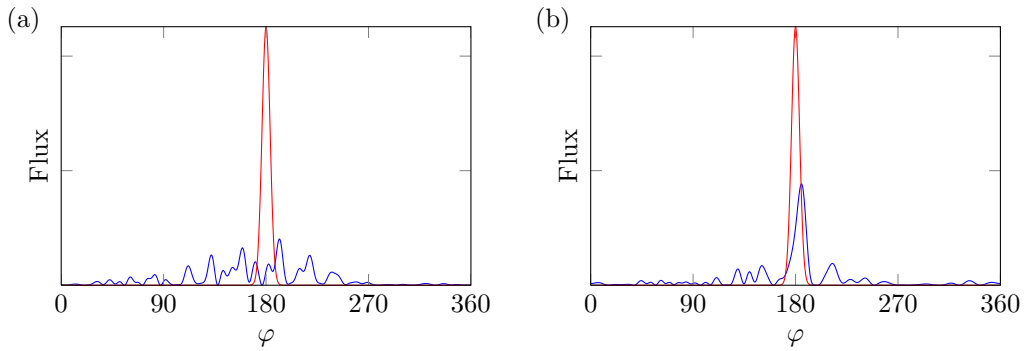
Figure 4.10.: Comparison of the directionalities $\mathcal{D}$ of two different modes. The energy-flux of a mode (a) features no good directionality ($\mathcal{D} = 0.16$), but the mode (b) has a directionality of $\mathcal{D} = 0.47$. The red line shows the desired Gaussian reference far-field profile $G(\varphi)$ with a FWHM of 11.7° that is used for the calculation of the measure $\mathcal{D}$. Both the Gaussian function as well as the blue energy-flux profiles are normalized to 1 with respect to the norm $\int_0^{2\pi} f(\varphi) \mathrm{d}\varphi$, where f denotes either $G(\varphi)$ or Flux(φ).

4.7.2. Choices for the pump profile basis

The two-dimensional pump profile needs to be expanded in terms of problem-specific basis functions in order to use it in an optimization algorithm. These basis functions can be either discontinuous, e.g., when using a constant pump in each element of a rectangular grid, or continuous. Experimentally, pump profiles described with such basis function can be realized with the help of spatial light modulators (SLM), even discontinuous ones, as long as the pixel-density of the SLM is high enough [15, 32]. Since, a discontinuous pump profiles are not very common, we will focus on

continuous pump profiles in the following.

The basis we use consists of the eigenfunctions of the Helmholtz problem in polar coordinates

$$\nabla^2 u_i(r, \varphi) = -k_i^2 u_i(r, \varphi), \tag{4.8}$$

with the eigenvalues k_i^2 and the eigenfunctions u_i. In polar coordinates the index i is in fact a pair of two indices n and m [33], which is due to the two-dimensionality of the problem. The Dirichlet boundary condition is imposed on the boundary of the unit circle

$$u_{n,m}(r, \varphi)|_{r=1} = 0. \tag{4.9}$$

It is known from Sturm-Liouville theory that if this eigenvalue problem (EVP) has a Hermitian boundary condition, i.e., the EVP is Hermitian, then the eigenfunctions $u_{n,m}$ are orthogonal to each other and form a complete basis [34]. This basis has the advantage that due to the boundary condition the pump profile features no discontinuities at $r = 1$. Such a discontinuity creates an artificial step in the total dielectric function strongly influencing the directionality of the laser modes as we have observed in chapter 3 and section 4.5.

The eigenfunctions $u_{n,m}(r, \varphi)$ are given by

$$u_{n,m}(r, \varphi) = J_n(k_{n,m}r)e^{-in\varphi}, \tag{4.10}$$

where k_{nm} is the m-th root of the n-th Bessel-function J_n. Due to these roots of the Bessel-function the eigenfunction $u_{n,m}$ fullfills the boundary condtion (4.9). Note that the Neumann functions $N_n(k_{n,m}r)$ that are also part of the solutions of the Helmholtz EVP in Eq. (4.8) are rejected because of their divergent and hence unphysical behavior at the origin [35]. The functions in Eq. (4.10) also arise in the description of vibrational modes of a circular drum. Due to the Hermitian boundary condition (4.9) the eigenfunctions $u_{n,m}$ are orthogonal with respect to the relation

$$
\begin{aligned}
\langle u_{n',m'}|u_{n,m}\rangle &= \int_0^{2\pi} e^{i(n'-n)\varphi}\,\mathrm{d}\varphi \int_0^1 J_{n'}(k_{n',m'}r)J_n(k_{n,m}r)\,\mathrm{d}r \\
&= \pi\delta_{n,n'}\delta_{m,m'}[J_{n+1}(k_{n,m})]^2.
\end{aligned} \tag{4.11}
$$

It follows that any given complex continuous function $f(r, \varphi)$ defined inside the unit circle and that vanishes at $r = 1$ can be expressed as a linear combination of the functions $u_{n,m}(r, \varphi)$

$$f(r, \varphi) = \sum_{n,m} \alpha_{n,m} u_{n,m}(r, \varphi), \tag{4.12}$$

in which the complex coefficients $\alpha_{n,m}$ are determined from the overlap integral of the functions $u_{n,m}$ and f.

   As the pump profile needs to be positive, i.e., no absorption inside the pumped regions, we use the absolute square

$$F(r,\varphi) = |f(r,\varphi)|^2 = \left| \sum_{n,m} \alpha_{n,m} J_n(k_{n,m}r)e^{-in\varphi} \right|^2 \tag{4.13}$$

of the linear combination f as the pump profile in our calculations.

   Allowing all possible pump configurations that can be represented with Eq. (4.13) would require an infinite number of coefficients $\alpha_{n,m}$ and therefore an infinitely dense mesh for our calculations. In addition to that a physical pump with arbitrary small changes is not possible either. Consequently, we require that only the coefficients with small indices n and m are non-zero. Correspondingly we introduce two new parameters n_{max} and m_{max} that fix the number of non-zero coefficients so that we can rewrite the pump profile $F(r,\varphi)$ as

$$F(r,\varphi) = \left| \sum_{n=-n_{max}}^{n_{max}} \sum_{m=1}^{m_{max}} \alpha_{n,m} J_n(k_{n,m}r)e^{-in\varphi} \right|^2 . \tag{4.14}$$

   Fig. 4.11 shows two pump profiles with randomly chosen coefficients $\alpha_{n,m}$, in which the number of non-zero coefficients is different.
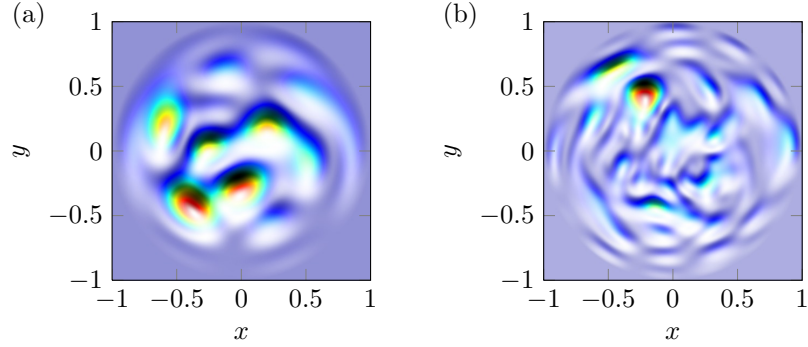
Figure 4.11.: Two random pump profiles $F(r,\varphi)$ (see Eq. (4.14)) described by 21 complex coefficients $\alpha_{n,m}$ ((a), $n_{max} = 3$, $m_{max} = 3$) and by 105 complex coefficients ((b), $n_{max} = m_{nax} = 7$).

4.7.3. Optimization process

Given the definition of the parametrized pump profile Eq. (4.14) we want to maximize the directionality $\mathcal{D}$ of the first TCF state by employing an optimization algorithm. The spatial variation of the pump profile should be in the scale of the

wavelength λ in order to be able to induce directional lasing modes. This is because for smooth variations of the pump profile the effect on the shaping of the spatial profile on the modes would not be as strong as for strongly varying spatial pump profiles. Therefore a giant search space is required, consisting of roughly 200 real variables for the wavelengths considered in this thesis.

Due to the large size of the parameter space it is not realistic to search for a global maximum. Instead, we use multiple random initial pump configurations and search for local maxima of the directionality. Using this non-deterministic approach we aim to come as close as possible to the global maximum. It remains to be checked, however, how close we can really get to the global maximum for a given size of the parameter space.

Genetic algorithms are perfectly suited for optimization problems with a large parameter space. However, they require a far larger amount of function evaluations when they are compared with gradient-based algorithms [36]. This fact makes genetic algorithms inappropriate for our problem, even if they can rapidly locate good solutions when the dimensionality of the parameter space is large. In our case they are inappropriate because one function evaluation, i.e., computing the first TCF state of a large EVP for a given pump configuration and then its directionality, is costly. Therefore we only consider algorithms which can take advantage of additional gradient information, especially algorithms that offer the user to provide a function which computes the gradient.

The measure $\mathcal{D}$ that should be optimized has the property that it is discontinuous. This is because the absolute values of the eigenvalues of the TCF state could come close to each other and the order of the TCF states eventually switch for certain pump configuration(s). The mode profile of the TCF states are in general very different from each other and so are their directionalities $\mathcal{D}$. As a consequence, the directionality of the first TCF state could jump for slight variations of the pump profile, resulting in a step of the gradient.

The gradient of the directionality can only be calculated numerically. In order to calculate it we replace the first TCF state that enters the measure $\mathcal{D}$ with a locally smooth approximation with the help of perturbation theory that was developed with the help of Florian Mintert. The employment of perturbation theory dramatically reduces the runtime of the optimization algorithm. However, the smooth approximation leads to errors but they can be neglected for our problem as long as they are small. This is the case for sufficiently small deviations of the pump profile $F(\mathbf{x})$.

We calculate the gradient with the forward-difference formula

$$\nabla_j \mathcal{D}(\{\alpha_i\}) = \frac{\mathcal{D}(\{\alpha_i\} + \Delta \hat{\mathbf{e}}_{\mathbf{j}}) - \mathcal{D}(\{\alpha_i\})}{\Delta}, \tag{4.15}$$

where $\Delta \hat{\mathbf{e}}_{\mathbf{j}}$ represents a shift of the j-th parameter α_j by Δ. Using perturbation theory only one EVP needs to be solved to calculate the whole gradient at the

current pump configuration. The j-th perturbed first TCF state and its expansion coefficients c_n are given by (for a derivation see Appendix B)

$$u_0[F(\{\alpha_i\} + \Delta \hat{\mathbf{e}}_{\mathbf{j}})] \approx u_0[F(\{\alpha_i\})] + \sum_{n=1}^{N} c_n u_n[F(\{\alpha_i\})], \tag{4.16a}$$

$$c_n = \frac{\eta_0}{\eta_n - \eta_0} \Delta \int F(\{\alpha_i\}) u_n[F(\{\alpha_i\})] u_0[F(\{\alpha_i\})] \, \mathrm{d}\mathbf{x}. \tag{4.16b}$$

The optimization algorithm, which we use, is an unconstrained local minimization algorithm based on the Newton Conjugate Gradient method [37] and is implemented in the SciPy [38] optimization package. As we want to maximize the directionality $\mathcal{D}$ the minimization function has to be set to

$$g(\{\alpha_i\}) = -\mathcal{D}\left[u_0[F(\{\alpha_i\})]\right] \tag{4.17}$$

and the gradient (4.15) has to be substituted by its negative $-\nabla_i \mathcal{D}$.

In the current implementation of our optimization function we did not calculate the directionality of the first laser mode but the directionality of the first threshold constant flux state at the frequency of the gain center. This should be a good approximation in the weakly scattering regime but a detailed check on the validity of this approximation should be carried out. The reason for taking the first TCF state as the first lasing mode is that the computation of the first TLM is far more time-consuming than computing the TCF states at a single frequency.

4.7.4. Results for systems with $kR = 8$

To reduce the effort needed to calculate the optimal pump configuration we first consider a cavity with $kR = 8$ and $n_s = 1.2$ (see Fig. 4.12). For this cavity we use 20 random pump configurations each with $n_{max} = 3$ and $m_{max} = 4$ (see Eq. (4.14)), corresponding to 28 complex coefficients $\alpha_{n,m}$. These pump configurations act as the initial configuration for the optimization algorithm. To compute the gradient of the measure $\mathcal{D}$ the step size is set to $\Delta = 0.001$ and 150 states are used for the calculation of the perturbed TCF states Eq. (4.16).

First we want to compare how good the obtained directionalities are if the gradients are calculated with perturbation theory and if they are calculated exactly, i.e., $m_{max}(2n_{max} + 1) + 1$ eigenvalue problems are computed to calculate one gradient (see Eq. (4.15)). For each of the 20 created pump profile we start the optimization algorithm once with employed perturbation theory (PERT) and once with the exact calculation (EXACT). It is surprising that the optimization algorithm performs better in the PERT case for almost half of the used pump profiles and for the other pump profile the EXACT case performs better. The best obtained directionality in the PERT case is $\mathcal{D} = 0.662$ whereas in the EXACT case $\mathcal{D}$ is slightly better:
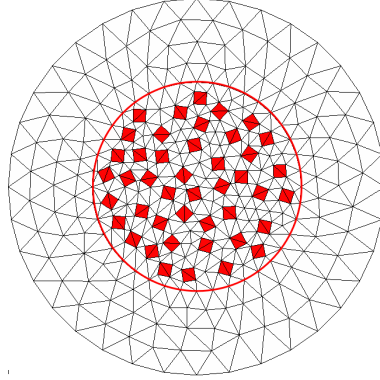
Figure 4.12.: Geometry of a two-dimensional random laser that is tuned to model random lasers with $kR = 8$. The coverage-rate f_{cov} is 0.2. The radius of the liquid gain medium is $R = 1.0$ and the diameter of the scatterers is $d_s = 0.17$. The red circle with $R = 1.0$ denotes the LSS.

$\mathcal{D} = 0.677$. These results are shown in Fig. 4.13. Even if the pump configurations look completely different the energy-flux of the first TCF state is similar. This suggests that the measure $\mathcal{D}$ features multiple local maxima. It should be noted that the initial pump configurations for the states in Fig. 4.13 are different, which could explain why the obtained pump profiles do not match. From the simulations made we can conclude that the perturbation theory performs well, even if an statistical ensemble with altogether 20 random initial pump configurations was not very large. In order to obtain good statistics for $kR = 8$ more pump profiles and different disorder potentials need to be considered.
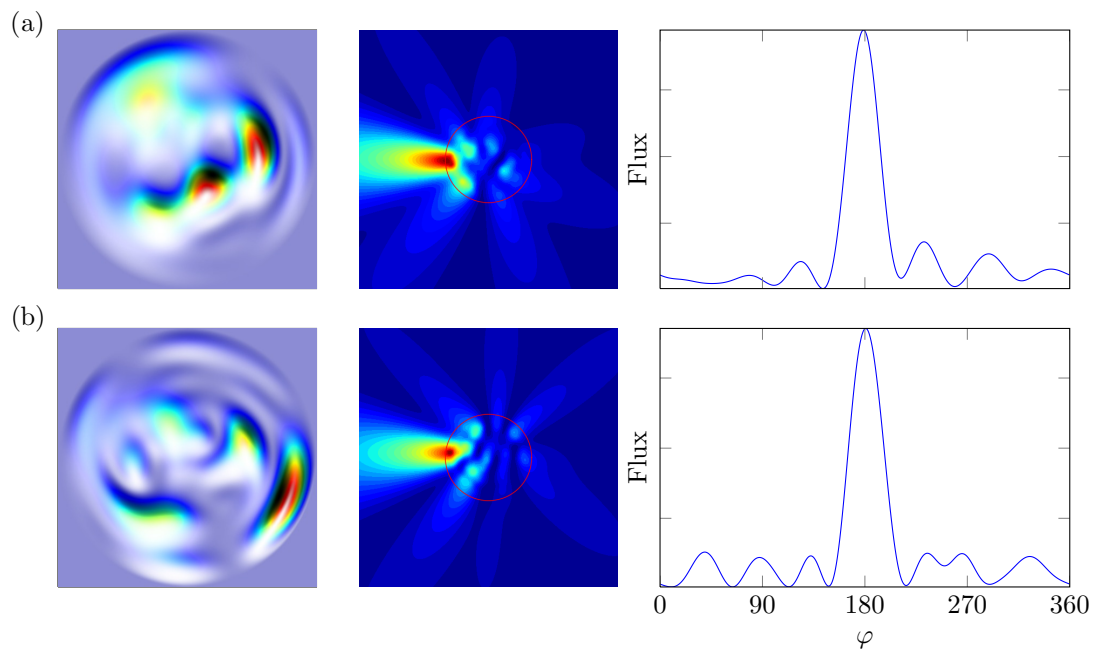
Figure 4.13.: Best results of the optimization algorithm for a cavity with $kR = 8$ and $n_s = 1.2$ (see Fig. 4.12) when (a) the gradient (4.15) is computed exactly and (b) the gradient is computed with the help of perturbation theory. Shown are the pump profile for the first TCF state and the energy-flux of this TCF state.

4.7.5. Results for systems with $kR = 30$

In the case of cavities with $kR = 30$ we again use 20 random pump configurations each with $n_{max} = 7$ and $m_{max} = 6$, corresponding to 90 complex coefficients $\alpha_{n,m}$. In the weakly scattering regime the best obtained value of the directionality $\mathcal{D}$ is 0.8889. In this case the algorithm started with an initial pump configuration (see Fig. 4.15 (a)) with a small directionality $\mathcal{D} = 0.007$, which shows that our optimization method works well. Considering the evolution of the measure $\mathcal{D}$ in Fig. 4.14 we see that it features negative peaks which are due to the mentioned mode switching. What is surprising is that for most of the peaks the directionality slightly above the peak positions is better than below. The overlap between the final energy-flux profile (at the last iteration step) and the reference far-field intensity is remarkably good. However, some pronounced side lobes (see Fig. 4.17) are visible, a feature which is expected as there is no confining structure involved.
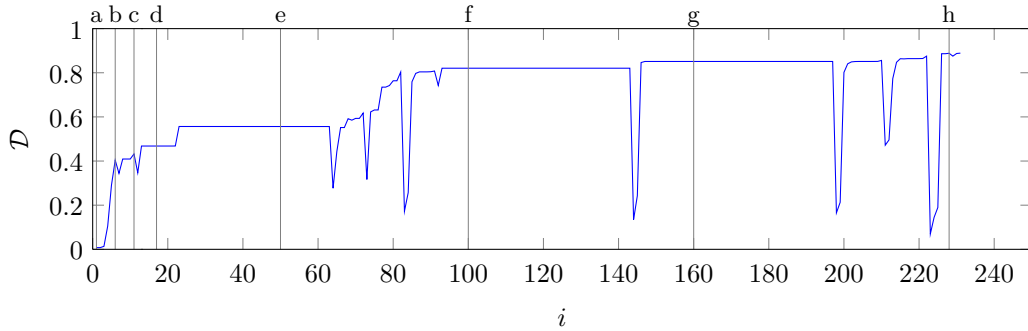
Figure 4.14.: Directionality $\mathcal{D}$ of a weakly scattering ($n_s = 1.2$) random laser as a function of the iteration step i, i.e., the number of evaluated gradients. The final value of $\mathcal{D}$ obtained after 231 iterations is 0.8889. The initial pump configuration is shown in Fig. 4.15(a). The pump configurations and the first TCF states at the labeled iteration steps (a-h) can be seen in Fig. 4.15 and Fig. 4.16.

If we increase the index of refraction of the scatterers and use the same generated random pump profiles (see Fig. 4.15) as the initial configuration for the optimization algorithm the best possible directionality $\mathcal{D}$ is decreasing, because the influence of the pump relative to the spatial index of refraction is decreasing. This is expected as for large indices of refraction the best value of $\mathcal{D}$ primarily depends on the directionality of the individual cavity modes. On the contrary, by decreasing the refractive index the results get even better, as is shown in the case of $n_s = 1.0$, i.e., no scatterers, in Fig. 4.18.
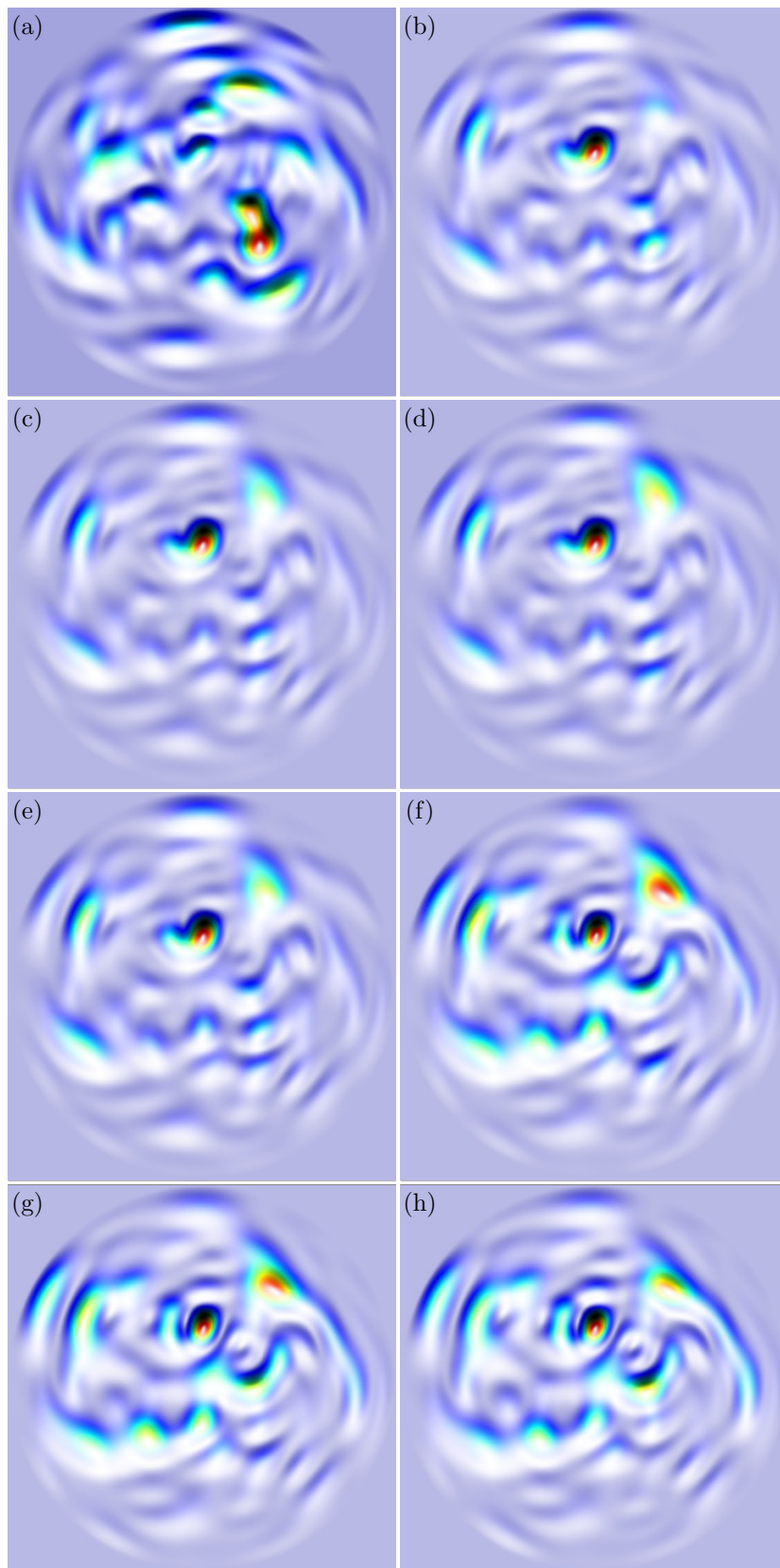
Figure 4.15.: Pump configurations at certain iterations steps (see Fig. 4.14) of the optimization algorithm.
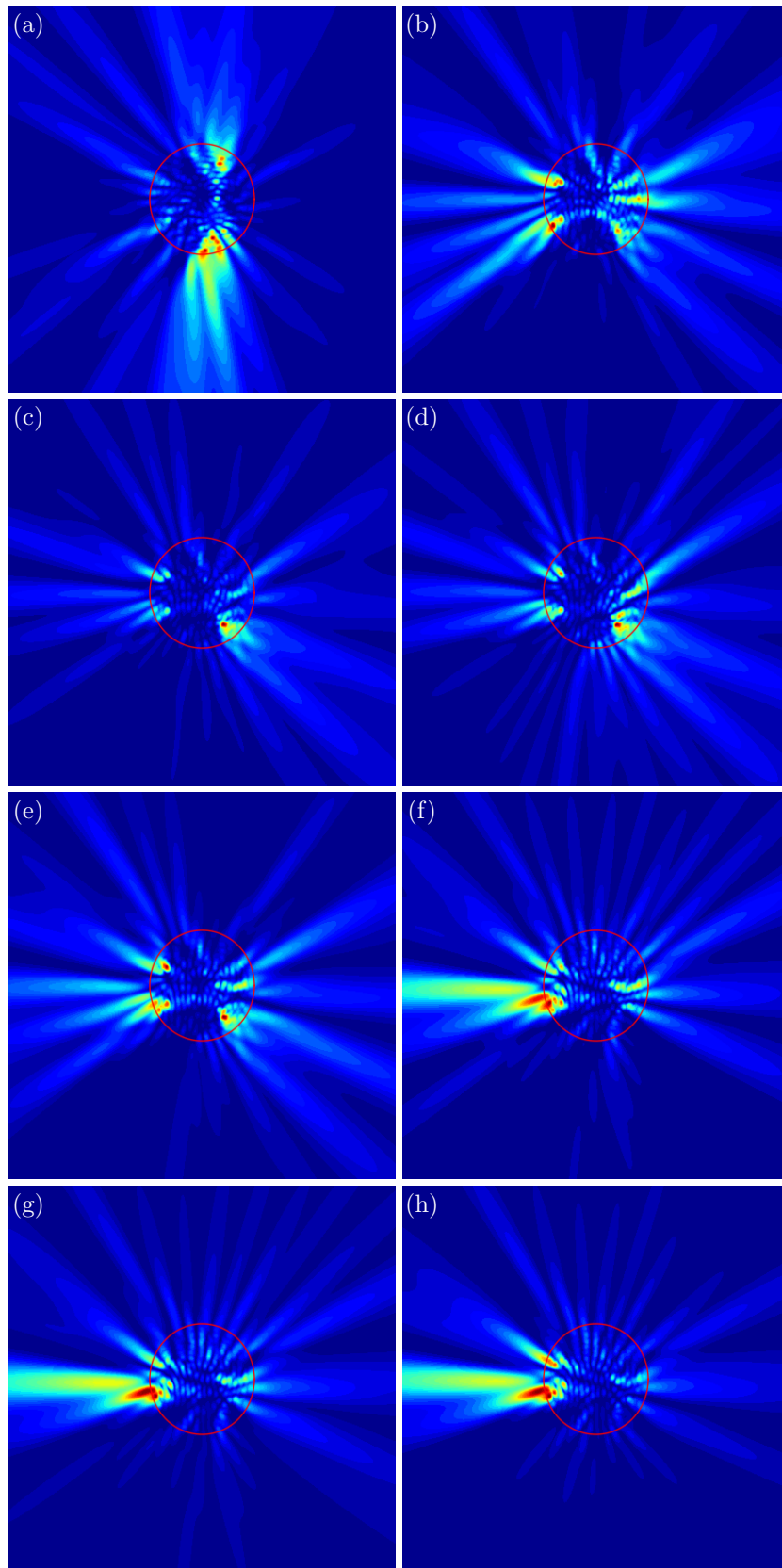
Figure 4.16.: First TCF states at certain iterations steps (see Fig. 4.14) of the optimization algorithm.
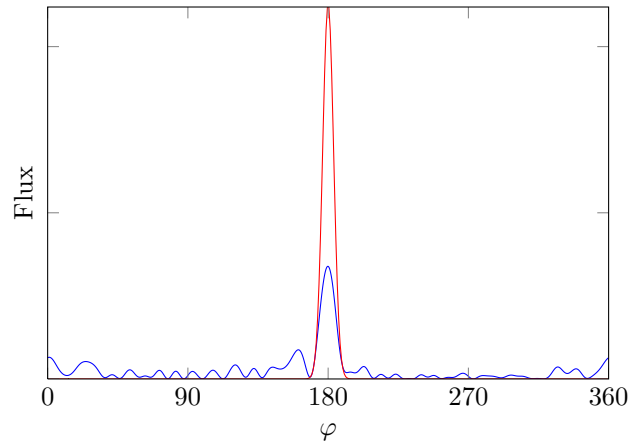
Figure 4.17.: Energy flux of the TCF state at the last iteration step ($i = 231$). The details are given in the caption of Fig. 4.14.
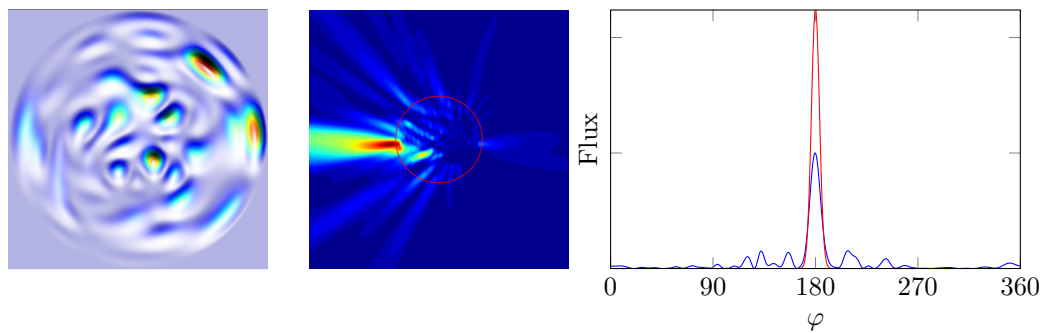
Figure 4.18.: Best obtained results for a cavity without scatteres ($n_s = 1.0$). Shown are the final pump configuration, the first TCF state and its energy-flux profile. The value of $\mathcal{D}$ is 0.9513.

Chapter 5.

Summary and outlook

In this thesis we studied how the directionality of non-interacting laser modes can be controlled by spatially varying the pump profile. In one-dimensional systems this task could be accomplished in low-Q cavities, where we found strongly directional laser modes by employing an optimization algorithm for the applied pump. In one-dimensional high-Q cavities the pump profile does not have a strong influence on the spatial profile of the modes compared to cavities with a low Q-factor. Therefore, already the passive high-Q cavity itself has to feature the desired directional modes, which we then select (mode-selection) with an appropriate pump configuration.

In two dimensions we observed a similar behavior in so-called random lasers which are composed of a multitude of scatterers embedded in a laser dye. If the scatterers are strongly reflective, the system is in the regime of strong (Anderson) localization. Here, only mode-selection is possible, but the selectable modes do in general not feature a pronounced directionality.

This is in contrast to the weakly scattering regime which we reach by decreasing the disorder strength. In this limit we can not only select but also shape the laser modes by varying the pump profile. These modes can be interpreted as modes of pump-induced cavities, which are created by the applied pump profile. First attempts to create such pump-induced modes by simply pumping the random laser with a profile that reflects a directional mode were not successful. Instead, we found that in the weakly scattering regime optimization algorithms can be applied to reach the goal of shaping directional modes.

For this purpose, we expanded the pump profile in terms of a Bessel function basis. The basis coefficients describing the pump profile were then tuned by the optimization algorithm. The huge parameter space (with ~ 200 real parameters) makes this optimization computationally very demanding, but with appropriate numerical techniques we were able to find very pronounced local optima starting from a multitude of initially random pump profile. Using this method we obtained pump profiles which feature first laser modes with strong directionality.

It has been shown very recently that exceptional points could lead to interesting new effects in laser systems as, e.g., situations in which a laser shuts down at a certain threshold but turns back on at a higher threshold [4]. Using the meth-

ods presented in this thesis to influence laser modes by spatially varying the pump configuration one could extend our work to study exceptional points in the pump-dependence of random lasers. In the case of 1D random lasers systems, recent experimental measurements conducted at the Institut Langevin, ESPCI Paristech showed that tuning of the laser mode with optimized pump profiles can be achieved [10]. We are thus optimistic that our numerical results on pump-controlled random lasers can be experimentally verified in the near future.

Acknowledgements

First and foremost I would like to express my gratitude to my advisor Prof. Stefan Rotter for his guidance, for fruitful discussions and for the chance he gave me to start this exciting thesis. Besides Stefan, I would also like to thank my officemate Matthias Liertzer, who always helped me when I had any kind of physical and software related problem.

Many thanks to my family for their financial support over the years and that they strengthened me to study physics. My girlfriend, Susanne, who was always full of good cheer and love, has provided me with indispensable encouragement, for which I am very thankful. Finally I thank those who I forgot to mention and apologize.

Appendix A.

Calculation of TCF states of one-dimensional edge-emitting laser-cavities

In this appendix we show how to calculate TCF states of various one-dimensional cavities. The cavities we consider consist of a finite stack of dielectric layers, each having a spatially constant index of refraction. In addition to that the refractive index is assumed to be frequency independent. Each index can both be real (i.e. neither loss nor gain inside the layer) or complex. The cavity edges are either connected to the medium of the environment (i.e. open boundary condition), or are terminated by a perfect mirror (i.e. Dirichlet boundary condition).

A.1. Single-layer laser cavity

The cavity shown in Fig. A.1 consists of a homogeneous medium of index n_0 and is closed on the left side ($x = 0$) and open on the right ($x = L_c$). In this simple case the laser only emits into the positive x-direction, which translates into the following boundary conditions for the TCF states

$$\partial_x u|_{x=L_c} = in_e k u|_{x=L_c}, \tag{A.1a}$$

$$u|_{x=0} = 0. \tag{A.1b}$$

Here, the cavity boundary ($x = L_c$) acts as the LSS. Hence, the TCF states u_m of such a cavity are defined by the eigenvalue problem

$$(\nabla^2 + n_0^2 k^2) u_m(x; k) = -\eta_m k^2 F(x) u_m(x; k), \qquad 0 < x \leq L_c \tag{A.2a}$$

$$(\nabla^2 + n_e^2 k^2) u_m(x; k) = 0, \qquad x > L_c, \tag{A.2b}$$

where n_0 is the index of the amplifying medium with length L_c, n_e the index of the environment, η_m is the TCF eigenvalue and $F(x)$ represents the pump profile. The solution outside the cavity (A.2b) is $A_m e^{in_e kx}$ and A_m is determined by the continuity condition of u_m and its first derivative.
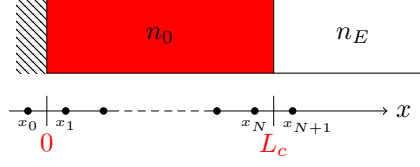
Figure A.1.: Homogeneous laser cavity of length L_c. The cavity medium with in-
dex n_0 is embedded into a semi-infinite medium n_e. At the bottom
an equidistant grid with spacing Δ is shown, which is used for the
numerical calculation of the TCF states (see Section A.3) in 1D.

A.2. Multi-layer laser cavity

In this thesis we simulate cavities consisting of a finite number of non-amplifying
dielectric layers attached to the gain-medium (see Fig. A.2). As for the single-
layer case the outgoing boundary condition needs to be fulfilled outside the LSS for
$(x > L_c)$, which is the same as for Eq. (A.1), assuming n_e is constant. Note, that
in the single-layer case the length of the gain region L_g and the length of the cavity
L_c are the same.
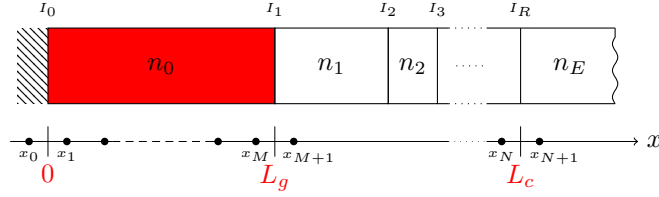
Figure A.2.: Laser cavity with a single gain region and multiple dielectric layers
attached to the right side of the gain region. All layers $n_1, n_2, \ldots, n_m$
have a real index of refraction. L_g denotes the length of the gain region
and L_c the length of the whole cavity. A hard wall boundary condition
is imposed on the left edge.

In addition to the boundary condition (A.1) the TCF states need to fulfill a con-
tinuity condition at all interfaces I_i (see Fig. A.2). The TCF states of such a multi-
layer laser cavity are given by,

$$
\begin{aligned}
(\nabla^2 + n_0^2 k^2)u_m(x;k) &= -\eta_m F(x)u_m(x;k), & 0 < x \leq L_g = x(I_1) \\
(\nabla^2 + n_i^2 k^2)u_m(x;k) &= 0, & x(I_i) < x \leq x(I_{i+1}) \\
(\nabla^2 + n_e^2 k^2)u_m(x;k) &= 0, & x > L_c.
\end{aligned}
\tag{A.3}
$$

Outside the gain region the general solutions can be calculated analytically

$$
\begin{aligned}
u_m(x;k) &= && a_i e^{ikn_i x} + b_i e^{-ikn_i x} && x(I_i) < x \le x(I_{i+1}) \\
u_m(x;k) &= && a_R e^{ikn_{i+1}x} + b_R e^{-ikn_{i+1}x} && x > L_c,
\end{aligned}
\tag{A.4}
$$

where a_i, a_R (b_i, b_R) are the complex coefficients of the right- (left-) propagating plane waves. Note that b_R needs to be zero as the lasing modes are purely outgoing.

A.3. Discretization technique

In order to calculate the TCF states for one-dimensional structures the finite difference method (FDM) is employed. The grid that we use is shown in the bottom half of Fig. A.1 and Fig. A.2. For simplicity we use a constant grid-spacing Δ to represent the entire cavity. This grid spacing is chosen to be much smaller than the smallest wavelength inside the cavity, hence by the highest index of refraction of one of its dielectric layers. This could waste computational resources if the total length of the layers with a high index of refraction is far smaller than the total length of the cavity. To overcome this problem the 1D finite element method (FEM) method can be applied. If the layers at the end of the cavity are non-amplifying a more efficient method is to discretize only the amplifying medium/media and incorporate the outer non-amplifying media with the help of a transfer-matrix method [19] as described in the next section.

In this thesis we employ the FDM with a constant grid spacing Δ, which leads to the finite-difference equation for the TCF states

$$
\frac{u_{n+1} + u_{n-1} - 2u_n}{\Delta^2} + n_n^2 k^2 u_n = -\eta_m F_n k^2 u_n,
\tag{A.5}
$$

where η_m is the eigenvalue of this equation and n_n, F_n and u_n are functions evaluated at the grid points x_n. Equation (A.5) is equivalent to a generalized eigenvalue problem $Au = \lambda Bu$ with the discretized boundary conditions for the two presented cavities

$$
u(x=0) = \frac{u_0 + u_1}{2} \quad \equiv \quad 0,
\tag{A.6}
$$

$$
u'(x=L_c) = \frac{u_{N+1} - u_N}{\Delta} \quad \equiv \quad ikn_e \frac{u_{N+1} + u_N}{2}.
\tag{A.7}
$$

Using these boundary conditions we can introduce a new frequency dependent constant β for each boundary which is given by

$$
u_0 = \underbrace{-1}_{\beta_l} u_1, \quad u_{N+1} = \underbrace{\frac{2 + in_e k\Delta}{2 - in_e k\Delta}}_{\beta_r} u_N
\tag{A.8}
$$

The linear relation between the function values u_0, u_1 and u_N, u_{N+1} allows us to write the Laplacian in Eq. (A.5) as

$$\frac{1}{\Delta^2} \begin{pmatrix} \beta_l - 2 & 1 & & & \\ 1 & -2 & 1 & & \\ & & \ddots & \ddots & \ddots & \\ & & 1 & -2 & 1 \\ & & & 1 & \beta_r - 2 \end{pmatrix} \tag{A.9}$$

A.4. Transfer matrix method

If the cavity includes a single or multiple non-amplifying dielectric layer(s) as in Fig. A.2, we can save in computational costs not by discretizing the layers but instead by effectively reducing them to a complex and frequency dependent reflection coefficient. This analytically calculated reflection coefficient can be incorporated into a new boundary condition imposed on the edge of the gain medium ($x = L_g$) replacing (A.7). To derive this boundary condition we introduce the transfer matrix $\hat{T}_{n_{i+1} \leftarrow n_i}$ which connects the complex wave amplitudes (a_{i+1}, b_{i+1}) with the amplitudes (a_i, b_i)

$$\hat{T}_{n_{i+1} \leftarrow n_i} = \frac{1}{n_{i+1}} \begin{pmatrix} e^{ik(n_i - n_{i+1})I_{i+1}}(n_{i+1} + n_i) & e^{ik(-n_i - n_{i+1})I_{i+1}}(n_{i+1} - n_i) \\ e^{ik(n_i + n_{i+1})I_{i+1}}(n_{i+1} - n_i) & e^{ik(n_{i+1} - n_i)I_{i+1}}(n_{i+1} + n_i) \end{pmatrix}. \tag{A.10}$$

The transfer matrix from layer 1 (wave amplitudes a_1, b_1) to the environment with index n_e (wave amplitudes a_R, b_R) can be written as the product

$$\hat{T}_{n_e \leftarrow n_1} = \hat{T}_{n_e \leftarrow n_{R-1}} \cdots \hat{T}_{n_3 \leftarrow n_2} \hat{T}_{n_2 \leftarrow n_1} \tag{A.11}$$

Using the fact that the outgoing boundary condition (A.7) is equivalent to $b_R = 0$ (no incoming waves from the right side) one obtains that the amplitudes in medium 1 are connected like

$$\frac{-T_{21}}{T_{22}} a_1 = b_1, \tag{A.12}$$

where T_{21} and T_{22} are elements of the two-dimensional matrix $\hat{T}_{n_e \leftarrow n_1}$. Substituting Eq. (A.12) into the continuity condition of the TCF state at I_1 leads to

$$\begin{aligned} u(x = I_1 = L_g) &\approx \frac{u_{N+1} + u_N}{2} \\ &\equiv a_1 e^{ikn_1 L_g} + b_1 e^{-ikn_1 L_g} \\ &= a_1 \left(e^{ikn_1 L_g} - \frac{T_{21}}{T_{22}} e^{-ikn_1 L_g} \right), \end{aligned} \tag{A.13}$$

and its first derivative

$$
\begin{aligned}
u'(x = L_g) \quad &\approx \quad \frac{u_{N+1} - u_N}{\Delta} \\
&\equiv \quad ikn_1(a_1 e^{ikn_1 L_g} - b_1 e^{-ikn_1 L_g}) \\
&= \quad ikn_1 a_1 (e^{ikn_1 L_g} + \frac{T_{21}}{T_{22}} e^{-ikn_1 L_g}).
\end{aligned}
\tag{A.14}
$$

The amplitude a_1 can be eliminated using Eqs. (A.13) and (A.14) and after some algebraic transformations one obtains

$$
u_{N+1} = \underbrace{\frac{2 + ikn_1\gamma}{2 - ikn_1\gamma}}_{\beta} u_N, \quad \gamma := \frac{1 - re^{-2ikn_1 L_g}}{1 + re^{-2ikn_1 L_g}},
\tag{A.15}
$$

where r is defined as the complex reflection coefficient

$$
r := b_1/a_1 = -T_{21}/T_{22}.
\tag{A.16}
$$

The calculation of the lasing modes of the one-dimensional cavity presented in section 3.2 can be sped by employing this technique.

Appendix B.

First order pertubation theory for symmetric non-Hermitian generalized eigenvalue problems

The presented perturbation theory was developed with the help of Florian Mintert. If the operator B of the given non-Hermitian generalized eigenvalue problem

$$Ax_i = \lambda_i B x_i \tag{B.1}$$

is perturbed by a small symmetric perturbation $\varepsilon \delta B$ the eigenvalues and eigenvectors shift and can be expressed in terms of a power series in ϵ. In this appendix we use first order pertubation theory in which the eigenvalue problem is given by

$$A(x_i + \epsilon \delta x_i) = (\lambda_i + \epsilon \delta \lambda_i)(B + \epsilon \delta B)(x_i + \epsilon \delta x_i), \tag{B.2}$$

in which we define the perturbed eigenstate in first order as

$$\delta x_i := \sum_{j \neq i} \alpha_j x_j. \tag{B.3}$$

By only considering the terms of Eq. (B.2) that are linear in ϵ we derive

$$(A - \lambda_i B)\delta x_i = (\delta \lambda_i + \lambda_i \delta B)x_i \tag{B.4}$$

The next step for the derivation of the perturbed eigenvalue and eigenstate is to substitute Eq. (B.3) into Eq. (B.2) and employ Eq. (B.1).

$$
\begin{aligned}
(A - \lambda_i B) \sum_{j \neq i} \alpha_j x_j \;\; &= \;\; \sum_{j \neq i} \alpha_j \left[A + (\underbrace{-\lambda_j + \lambda_j}_{0} - \lambda_i) \right] B x_j && \text{(B.5)} \\
&= \;\; \sum_{j \neq i} \alpha_j \left[\underbrace{(A - \lambda_j B) x_j}_{0} + (\lambda_j - \lambda_i) \right] B x_j \\
&= \;\; \sum_{j \neq i} \alpha_j (\lambda_j - \lambda_i) B x_j \\
&\overset{!}{=} \;\; (\delta\lambda_i B + \lambda_i \delta B) x_i
\end{aligned}
$$

Multiplying Eq. (B.5) from the left by the transpose of the unperturbed state x_j results in

$$
\sum_{j \neq i} \alpha_j (\lambda_j - \lambda_i) x_j^T B x_i = \delta\lambda_i \underbrace{x_i^T B x_i}_{1} + \lambda_i x_i^T \delta B x_i. \tag{B.6}
$$

Due to the biorthogonality of the eigenstates of Eq. (B.1) the perturbation of the i-th eigenvalue follows from Eq. (B.6) and is given by

$$
\delta\lambda_i = -\lambda_i x_i^T \delta B x_i. \tag{B.7}
$$

Analogously, if Eq. (B.6) is multiplied from the left by x_j^T, where $j \neq i$

$$
\alpha_j (\lambda_j - \lambda_i) \underbrace{x_j^T B x_j}_{1} = \delta\lambda_i \underbrace{x_j^T B x_i}_{0} + \lambda_i x_j^T \delta B x_i, \tag{B.8}
$$

one obtains the expansion coefficients α_j of the i-th perturbed eigenstate $\tilde{x}_i$

$$
\alpha_j = \frac{\lambda_i}{\lambda_j - \lambda_i} x_j^T \delta B x_i \tag{B.9a}
$$

$$
\tilde{x}_i = x_i + \sum_{j \neq i} \alpha_j x_j \tag{B.9b}
$$

The obtained expression (B.9b) for the perturbed eigenvector is used to calculate the perturbed TCF states for slight variations of the pump profile required for efficiently computing the gradient of the measure $\mathcal{D}$ (see Section 4.7.3).

Bibliography

[1] Anthony E. Siegman. *Lasers*. University Science Books, 1st edition edition, May 1986.

[2] Hakan E. Türeci, A. Douglas Stone, and B. Collier. Self-consistent multimode lasing theory for complex or random lasing media. *Phys. Rev. A*, 74(4):043822, October 2006.

[3] Li Ge, Y. D. Chong, and A. Douglas Stone. Steady-state ab initio laser theory: Generalizations and analytic results. *Phys. Rev. A*, 82(6):063824, December 2010.

[4] M. Liertzer, Li Ge, A. Cerjan, A. D. Stone, H. E. Türeci, and S. Rotter. Pump-Induced exceptional points in lasers. *Phys. Rev. Lett.*, 108:173901, April 2012.

[5] Chang H. Yi, Myung W. Kim, and Chil M. Kim. Lasing characteristics of a lima[c-cedilla]on-shaped microcavity laser. *Applied Physics Letters*, 95(14):141107, 2009.

[6] Changling Yan, Qi J. Wang, Laurent Diehl, Martina Hentschel, Jan Wiersig, Nanfang Yu, Christian Pflügl, Federico Capasso, Mikhail A. Belkin, Tadataka Edamura, Masamichi Yamanishi, and Hirofumi Kan. Directional emission and universal far-field behavior from semiconductor lasers with lima[c-cedilla]on-shaped microcavity. *Applied Physics Letters*, 94(25):251101, 2009.

[7] Q. H. Song, L. Ge, A. D. Stone, H. Cao, J. Wiersig, J. B. Shim, J. Unterhinninghofen, W. Fang, and G. S. Solomon. Directional laser emission from a Wavelength-Scale chaotic microcavity. *Phys. Rev. Lett.*, 105(10):103902, August 2010.

[8] Susumu Shinohara, Takahisa Harayama, Takehiro Fukushima, Martina Hentschel, Satoshi Sunada, and Evgenii E. Narimanov. Chaos-assisted emission from asymmetric resonant cavity microlasers. *Phys. Rev. A*, 83:053837, May 2011.

[9] Qi J. Wang, Changling Yan, Nanfang Yu, Julia Unterhinninghofen, Jan Wiersig, Christian Pflügl, Laurent Diehl, Tadataka Edamura, Masamichi Yamanishi, Hirofumi Kan, and Federico Capasso. Whispering-gallery mode resonators

for highly unidirectional laser action. *Proceedings of the National Academy of Sciences*, 107(52):22407–22412, December 2010.

[10] Nicolas Bachelard, Jonathan Andreasen, Sylvain Gigan, and Patrick Sebbah. Taming random lasers through active spatial control of the pump. February 2012.

[11] H. E. Türeci and A. D. Stone. Mode competition and output power in regular and chaotic dielectric cavity lasers. 2005.

[12] Diederik S. Wiersma. The physics and applications of random lasers. *Nat. Phys.*, 4(5):359–367, May 2008.

[13] H. Cao, Y. Ling, J. Y. Xu, A. L. Burin, and R. P. H. Chang. Lasing with resonant feedback in random media. *Physica B: Condensed Matter*, 338(1-4):215–218, October 2003.

[14] David J. McCabe, Ayhan Tajalli, Dane R. Austin, Pierre Bondareff, Ian A. Walmsley, Sylvain Gigan, and Beatrice Chatel. Spatio-temporal focusing of an ultrafast pulse through a multiply scattering medium. *Nat Commun*, 2:447, August 2011.

[15] E. G. van Putten, D. Akbulut, J. Bertolotti, W. L. Vos, A. Lagendijk, and A. P. Mosk. Scattering lens resolves sub-100˜nm structures with visible light. *Phys. Rev. Lett.*, 106(19):193905, May 2011.

[16] I. M. Vellekoop and A. P. Mosk. Universal optimal transmission of light through disordered materials. *Phys. Rev. Lett.*, 101(12):120601, September 2008.

[17] Jochen Aulbach, Bergin Gjonaj, Patrick M. Johnson, Allard P. Mosk, and Ad Lagendijk. Control of light transmission through opaque scattering media in space and time. *Phys. Rev. Lett.*, 106:103901, March 2011.

[18] Hermann Haken. *Laser Light Dynamics, Volume II*. North Holland, 1 edition, December 1986.

[19] L. Ge. *Steady-state ab initio laser theory and its applications in random and complex media*. PhD thesis, Yale University, 2010.

[20] Matthias Liertzer. Nonlinear interactions in coupled microlasers. Master's thesis, UT Vienna, 2011.

[21] Hakan E. Türeci, Li Ge, Stefan Rotter, and A. Douglas Stone. Strong interactions in multimode random lasers. *Science*, 320(5876):643–646, May 2008.

[22] P. L. Kapur and R. Peierls. The dispersion formula for nuclear reactions. *Proc. R. Soc. London, Ser. A*, 166(925), 1938.

[23] John D. Jackson. *Classical Electrodynamics Third Edition*. Wiley, 3 edition, August 1998.

[24] Orazio Svelto. *Principles of Lasers*. Springer, 4th edition, September 2009.

[25] Li Ge, Y. D. Chong, S. Rotter, H. E. Türeci, and A. D. Stone. Unconventional modes in lasers with spatially varying gain and loss. *Phys. Rev. A*, 84(2):023820, August 2011.

[26] Karl F. Renk. *Basics of Laser Physics: For Students of Science and Engineering (Graduate Texts in Physics)*. Springer, 2012 edition, February 2012.

[27] A. E. Siegman. Laser beams and resonators: the 1960s. *IEEE Journal of Selected Topics in Quantum Electronics*, 6(6):1380–1388, November 2000.

[28] J. Andreasen, A. A. Asatryan, L. C. Botten, M. A. Byrne, H. Cao, L. Ge, L. Labonté, P. Sebbah, A. D. Stone, H. E. Türeci, and C. Vanneste. Modes of random lasers. *Adv. Opt. Photon.*, 3(1):88–127, March 2011.

[29] Matthias Liertzer. Private communication, 2012.

[30] Oliver Wright. Gallery of whispers. *PhysicsWorld*, pages 31–36, February 2012.

[31] Stefano Gottardo, Riccardo Sapienza, Pedro D. Garcia, Alvaro Blanco, Diederik S. Wiersma, and Cefe Lopez. Resonance-driven random lasing. *Nature Photonics*, 2(7):429–432, June 2008.

[32] S. M. Popoff, G. Lerosey, R. Carminati, M. Fink, A. C. Boccara, and S. Gigan. Measuring the transmission matrix in optics: An approach to the study and control of light propagation in disordered media. *Phys. Rev. Lett.*, 104(10):100601, March 2010.

[33] Kwong-Tin Tang. *Mathematical Methods for Engineers and Scientists 3: Fourier Analysis, Partial Differential Equations and Variational Methods (v. 3)*. Springer, 1 edition, February 2007.

[34] Philip M. Morse and Herman Feshbach. *Methods of Theoretical Physics, Part II*. Mcgraw-Hill College, first edition, June 1953.

[35] George B. Arfken, Hans J. Weber, and Frank E. Harris. *Mathematical Methods for Physicists, Seventh Edition: A Comprehensive Guide*. Academic Press, 7 edition, January 2012.

[36] David W. Zingg, Marian Nemec, and Thomas H. Pulliam. A comparative evaluation of genetic and gradient-based algorithms applied to aerodynamic optimization. *Revue européenne de mécanique numérique*, 17(1-2):103–126, March 2008.

[37] Jorge Nocedal and Stephen Wright. *Numerical Optimization (Springer Series in Operations Research and Financial Engineering)*. Springer, 2nd edition, July 2006.

[38] Jones Eric, Oliphant Travis, and Peterson Pearu. SciPy: Open source scientific tools for Python, 2001.